# Simulations of convection with crystallization in the system KAlSi$_2$O$_6$-CaMgSi$_2$O$_6$: Implications for compositionally zoned magma bodies

FRANK J. SPERA, CURTIS M. OLDENBURG, CONSTANCE CHRISTENSEN, MICOL TODESCO

Department of Geological Sciences and the Institute for Crustal Studies, University of California,
Santa Barbara, California 93106, U.S.A.

## ABSTRACT

A model has been developed and applied to study the origin of compositional and phase heterogeneity in magma bodies undergoing simultaneous convection and phase change. The simulator is applied to binary-component solidification of an initially superheated and homogeneous batch of magma. The model accounts for solidified, mushy (two- or three-phase), and all-liquid regions self-consistently, including latent heat effects, percolative flow of melt through mush, and the variation of system enthalpy with composition, temperature, and solid fraction. Phase equilibria and thermochemical and transport data for the system KAlSi$_2$O$_6$-CaMgSi$_2$O$_6$ were utilized to address the origin of compositional zonation in model peralkaline magmatic systems. Momentum transport is accomplished by Darcy percolation in solid-dominated regions and by internal viscous stress diffusion in melt-dominated regions within which relative motion between solid and melt is not allowed. Otherwise, the mixture advects as a pseudofluid with a viscosity that depends on the local crystallinity. Energy conservation is written as a mixture-enthalpy equation with subsidiary expressions that are based on thermochemical data and phase relations that relate the mixture enthalpy to temperature, composition, and phase abundances at each location. Species conservation is written as the low-density component (KAlSi$_2$O$_6$) and allows for advection and diffusion as well as the relative motion between solid and melt.

Systematic simulations were performed to assess the role of thermal boundary conditions, solidification rates, and magma-body shape on the crystallization history. Examination of animations showing the spatial development of the bulk (mixture) composition ($C$), melt composition ($C_1$), temperature ($T$), solid fraction ($f_s$), mixture enthalpy ($h$), and velocity ($\mathbf{V}$), reveals the unsteady and complex nature of convective solidification owing to nonlinear coupling among the momentum, energy, and species conservation equations. A consequence of the coupling includes the spontaneous development of compositional heterogeneity in terms of the modal abundances of diopside and leucite in the all-solid parts of the domain (i.e., modal mineralogical heterogeneity) as well as spatial variations in melt composition particularly within mushy regions where phase relations strongly couple compositional and thermal fields. Temporal changes in the rate of heat extraction because of bursts of crystallization and concomitant buoyancy generation are also found. Crystallization of diopside, the liquidus phase in all cases, enriches residual melt in low-density K-rich liquid. The upward flow of this material near the mush-liquid interface leads to the development of a strong vertical compositional gradient. The main effect of magma-body shape and different thermal boundary conditions is in changing the rate of solidification; in all cases compositional heterogeneities develop. The rate of formation of the compositional stratification is highest for the sill-like body because of its high cooling rate. Compositional zonation in a fully solidified body is found to be both radial and vertical. The most salient feature of this simple model is the spontaneous development of large-scale magma heterogeneity from homogeneous and slightly superheated initial states, assuming local equilibrium prevails during the course of phase change.

## INTRODUCTION

One of the most important problems in igneous petrology is elucidation of the mechanisms that give rise to magmatic diversity. This problem is practically as old as the discipline itself, and it would be difficult to review the subject in a single contribution. An adequate critique would encompass the entire field of igneous petrology, include the history of planetary differentiation and crustal growth (e.g., Galer and Goldstein, 1991; Taylor and

McLennan, 1985), and draw upon geochemical data from hundreds if not thousands of ancient and modern magmatic centers.

Since the pioneering work of Bowen (1928), it has been generally accepted that crystal fractionation is one of the most effective magmatic differentiation processes. By some means, crystals become separated from the melts in which they crystallize. Despite the general significance of this problem, the mechanism of crystal fractionation and the associated question of the vigor of convection in magma bodies remain controversial (e.g., Marsh, 1989; Martin and Nokes, 1989; Gibb and Henderson, 1992; Huppert and Worster, 1992). The problem is challenging mainly because of the enormous changes in magma viscosity that occur in the crystallization interval. Although adequate models exist for the calculation of melt viscosity as a function of temperature and composition (e.g., Shaw, 1972; Bottinga and Weill, 1972; Urbain et al., 1982; see also Stein and Spera, 1993), accurate description of the complex rheological behavior of magmatic mixtures is a far more difficult task (Lejeune and Richet, 1995). Because, in general, there can be relative motion between the constituent solid, melt, and vapor phases and because component phases have such widely different physical properties, the characterization of the rheology of magmatic mixtures presents a formidable problem. Briefly stated, it is difficult to describe simply and accurately both the rheological properties of magma and the relationship between phase fraction (e.g., fraction solid, $f_s$) and permeability of magmatic multiphase mixtures across the wide range of conditions relevant to magma transport and evolution. The problem is particularly acute in silicic and intermediate-composition systems for which there is overwhelming and incontrovertible evidence that large volumes of evolved magma, sometimes exceeding several thousand cubic kilometers, exist within the crust. Furthermore, differentiation may occur at geologically rapid rates (e.g., $10^{-2}$ km³/yr) prior either to solidifying to form mineralogically zoned or layered plutons or other composite batholiths or to erupting to form compositionally zoned ignimbrites or lava flows (Smith, 1979; Hildreth, 1981; Trial and Spera, 1990; Wiebe, 1993). A classic example is the 600 km³ Bishop Tuff in eastern California (Hildreth, 1979) emplaced as a plinian pumice fall, followed by a sequence of pyroclastic flows. Hildreth concluded that no mixing of crystals by gravitational settling had occurred prior to the eruption. His conclusion was based principally on the observation that individual hand-sized pyroclasts had compositionally uniform populations of phenocrysts. Recently, Lu et al. (1992) compared the amount of crystallization in a single Bishop Tuff pyroclast inferred from trace element abundance patterns with that observed in the host pyroclast utilizing melt (glass) inclusions within quartz phenocrysts. They concluded that the trace element compositions of the melt inclusions span a range larger than explicable by in situ phenocryst crystallization within the pyroclast. The larger extent of crystallization inferred from trace element abundances is good

evidence that separation of crystals from melt had occurred, although the mechanism and rate by which this was accomplished are not constrained by the geochemical data. Evidently, the lack of interphenocryst chemical variation and correlation between phenocryst composition and enclosing melt (glass) composition argues against simple crystal settling. Similar conclusions were reached by Dunbar and Hervig (Dunbar and Hervig, 1992; Hervig and Dunbar, 1992) in their detailed study of melt-inclusion trace element abundances and comparisons with enclosing pumice and whole-rock compositions.

A popular scenario whereby compositionally evolved melt becomes separated from associated crystals is by marginal upflow, a mechanism first hypothesized by Shaw (1974) and extensively investigated theoretically, experimentally, and by numerical simulation since then (e.g., Turner, 1980; Chen and Turner, 1980; Turner and Gustafson, 1981; Spera et al., 1982, 1984, 1989; Huppert and Sparks, 1984; Turner, 1985; Nilson et al., 1985; McBirney et al., 1985; Lowell, 1985; Huppert et al., 1986; Bergantz and Lowell, 1987; Trial and Spera, 1988; Leitch, 1989; Langmuir, 1989; Huppert, 1990). The essential idea is that in systems where phase change occurs along a subvertical sidewall (e.g., solidification or anatexis), the initial downward flow of cooled marginal magma can be reversed if phase change enriches melt in low-density components (e.g., $SiO_2$, $Na_2O$, $K_2O$, and $H_2O$) sufficiently to overcome negative thermal buoyancy effects. In this model, accumulation by advective transport of the cooler but chemically enriched (and buoyant) melt at the top of the magma body produces a thermally and chemically zoned layer. Additional in situ crystallization within the roofward layer then produces a magmatic mixture with a phenocryst content inconsistent with any single-stage, closed-system fractionation scheme, but consistent with trends expected from crystal-fractionation processes as commonly noted (Michael, 1983; Wolff and Storey, 1984). If $H_2O$ is significantly enriched upward, then the local (compositionally dependent) liquidus to solidus temperature interval, as well as the liquidus temperature itself, varies with depth within the magma body. This leads to variation in phenocryst content with location within the body independent of the effects of crystal settling.

Although the simple version of the marginal upflow hypothesis is conceptually pleasing and there is no doubt that marginal upwelling occurs in laboratory experiments with aqueous solutions, its relevance to magma differentiation has been questioned (see review by Trial and Spera, 1990). To develop an evolved roofward layer, chemically induced buoyancy within the very thin chemical boundary layer must overcome negative buoyancy within the thicker sidewall thermal boundary layer. Detailed numerical simulations and scale analysis were used by Spera et al. (1989) to show that roofward enrichment of light component occurs only if a critical ratio of compositional to thermal buoyancy is exceeded. They found that this critical buoyancy ratio ($R\rho_c$) depends on the Lewis number ($Le$), defined as the ratio of thermal to chemical

diffusivity. For roofward enrichment to occur by sidewall upflow, the condition in a two-component single-phase melt is

$$R\rho_c > \tfrac{2}{9}Le^{2/3} \qquad (1)$$

where $R\rho \equiv \beta j_w k / \alpha q_w \rho D$, $Le \equiv \kappa/D$, and $\beta$, $j_w$, $k$, $\alpha$, $q_w$, $\rho$, $D$, and $\kappa$ represent the compositional expansivity of the melt, mass flux of rejected light component because of a phase change along the sidewall, magma thermal conductivity, isobaric thermal expansivity of the melt, heat flux into the country rock, magma density, chemical diffusivity of light component, and magma thermal diffusivity, respectively. This criterion is valid for a strictly one-phase fluid subject to marginal boundary conditions on mass ($j_w$) and heat ($q_w$) flux. If sidewall conditions are set on composition ($C_w$) and temperature ($T_w$) rather than on their fluxes, the appropriate inequality is

$$R\rho_c > 1.2Le^{1/3} \qquad (2)$$

where in this case $R\rho$ is defined $R\rho = \beta\Delta C / \alpha\Delta T$. Because the Lewis number for a typical oxide component in a silicate melt is $\geq 10^4$, $R\rho$ values on the order of 10–100 are necessary to enable upflow in magmatic situations. Application of these criteria suggests that the $SiO_2$ component, because of its small on-diagonal chemical diffusivity ($D \approx 10^{-16}$ m²/s), would not be significantly enriched upward, whereas $H_2O$ possibly could be. Details, including numerical examples, are provided in the studies of Trial and Spera (1988, 1990) and Spera et al. (1989).

Although Equations 1 and 2 are valid criteria governing the conditions for upflow, the limitations of the model must be kept in mind if one seeks to explain magma differentiation. Perhaps the most significant limitation is that phase change (e.g., solidification or assimilation) along the margin is not explicitly taken into account. In simple models (Shaw, 1974; Spera et al., 1984; Nilson et al., 1985; Lowell, 1985; McBirney et al., 1985), one merely specifies that the wall temperature ($T_w$) and composition ($C_w$) or the boundary (wall) flux of light component ($j_w$) and heat flux ($q_w$) are time-independent, uncoupled boundary conditions. This is a useful procedure but is only an approximation. Heat and chemical transport through a marginal mush are not explicitly considered in these strictly one-phase models. Consequently, the effects of latent heat, the generation of compositionally distinct melt resulting from constraints imposed by phase relations, and the percolation of melt through the sidewall mush are not taken into account.

The single-phase approximation and hence the conditions for upflow represented by Equations 1 and 2 are valid provided the thickness of the multiphase region is small in comparison with the thickness of the thermal boundary layer, which is on the order of several meters. But it must be emphasized that firm quantitative constraints on the flux of mass ($j_w$) and heat ($q_w$) along the contacts between country rock and magma (or $C_w$ and $T_w$) are difficult to establish and probably highly variable. A proper accounting of the energetics and thermodynam-

ics of realistic silicate systems, including the rheological and permeability properties of mush, should also be made for the reasons cited earlier.

If the solidus to liquidus temperature interval is not small (the usual case), a significant thickness of mush would develop along marginal cooling surfaces (Bergantz and Lowell, 1987; Bergantz, 1992). This invalidates the criteria written as Equations 1 and 2. If positive compositional buoyancy exceeds negative thermal buoyancy, then upward-flowing, chemically enriched interstitial melt in a marginal two-phase mush zone may exist. The thickness of this mush is delimited by the liquidus and solidus isotherms. The vigor of the potential upflow that may occur depends on many factors. It is important to note that the upward flow of buoyant and chemically evolved melt is not diffusion limited in this case because buoyancy is generated by phase change everywhere within the mush. In this version of the marginal upflow hypothesis, one which is somewhat more realistic, the mush thickness and interstitial velocity of melt through the mush by percolative flow and rheological properties of the magmatic mixture are the critical factors. Diffusion through the melt is of minor importance because the thickness of the chemically enriched region is governed by the complicated feedback between the rate of marginal crystallization and phase relations, particularly the relationship among the mixture enthalpy, temperature, and composition. This feedback includes latent heat effects associated with phase change and the differential velocity of solid and melt within the mushy region. The rheological transition between solid-dominated and melt-dominated magma is also critically important.

With the above comments in mind, the purpose of this study can be given. We have developed an algorithm (Oldenburg and Spera, 1990, 1991, 1992a, 1992b) that considers simultaneous phase change (melting and solidification) and convection in two-component multiphase systems to model convection in a binary eutectic system undergoing crystallization. This model accounts for solidified, mushy, and all-liquid regions in a self-consistent manner, including latent heat effects, flow of melt through permeable mush, and the variation of system (melt plus solid) enthalpy with composition, temperature, and fraction solid ($f_s$). We used phase equilibria, thermochemical data, and transport data for the binary system $KAlSi_2O_6$ (leucite)–$CaMgSi_2O_6$ (diopside) in the simulations. Although we do not intend the calculations to be relevant to a particular ignimbrite, the results are relevant to the origin of compositionally zoned peralkaline magma (Wolff and Storey, 1984). As an example, one may cite the series of eight compositionally zoned phonolitic to trachytic ignimbrites erupted from the Somma-Vesuvius eruptive center in the last 2500 yr. Somma-Vesuvius is a classic example of a single magmatic center that has repeatedly emitted zoned magma (Joron et al., 1987). Elementary mass-balance crystal-fractionation models for these chemically zoned ignimbrites involve removal of leucite and clinopyroxene. The main purpose of the simulations

is to assess the likelihood that a boundary-layer flow can cause compositional zonation in the system $KAlSi_2O_6$-$CaMgSi_2O_6$ under boundary and initial conditions appropriate for the crystallization of phonolitic magma within the crust starting with a homogeneous, slightly superliquidus melt of appropriate bulk composition. We also investigated the role of convective macrosegregation with respect to the formation of a mineralogically zoned intrusive body following complete solidification.

The remainder of this paper is organized as follows. In the next section, a brief description of the model is presented in nonmathematical terms. This is followed by presentation of the mathematical model, including relevant initial and boundary conditions, phase equilibria, and melt-density relations in the system $KAlSi_2O_6$-$CaMgSi_2O_6$. The results of the simulations, including examination of the effects of magma-chamber aspect ratio, rate of cooling, and thermal boundary conditions, on the development of chemical differentiation are then given. The consequences of macrosegregation, especially with regards to mineralogical zonation in plutons, are discussed in the penultimate section. In the last section, the results are summarized and some speculations on the relevance of the simulations to the origin of magmatic diversity are offered.

# MODEL

## Overview

Unlike solidification of a single-component liquid, crystallization of magma is not characterized by the presence of a distinct front separating regions of solid and liquid (melt). Crystallization of multicomponent silicate melts gives rise to a permeable two-phase mushy region characterized by a microstructure that depends upon the conditions of solidification (e.g., rapid chilling, slow cooling, etc.) and the thermodynamic and transport properties of the material undergoing phase change. The thickness of the mushy zone, where $f_s$ varies between zero and one, is delimited by the liquidus and solidus isotherms, respectively. In a binary system at fixed pressure, the liquidus temperature depends on the local bulk composition, whereas the solidus temperature is constant and equal to the eutectic temperature. During phase change, latent heat released along the microscopic crystal-melt interface is redistributed within the mush by conduction and, when significant relative motion exists between solid and melt, by melt advection. Compositional variations arise because of differences in solubilities of components in coexisting melt and solids. Because of thermodynamic constraints on solidification as embodied by the equilibrium phase diagram, selective rejection of components also occurs along phase interfaces. This results in differences in melt density, which set up local buoyancy flows of thermal and compositional origin and, because gradients in chemical potential exist, concomitant diffusive flows (e.g., Morse, 1988).

In previous work (Oldenburg and Spera, 1991, 1992a,

1992b) we presented a two-dimensional continuum model of convection with phase change in which a single set of conservation equations for mass, momentum, energy, and species is applicable to all regions (solid, mush, and melt) in a binary eutectic system. The model is a modified version of the formulation developed by Bennon and Incropera (1987a, 1987b) and is closely related to similar formulations (Voller et al., 1989; Beckermann and Viskanta, 1988; Ni and Beckermann, 1991). This approach integrates semiempirical laws, a microscopic approach to transport processes in multiphase regions, and classical macroscopic mixture theory to achieve a quantitative description of crystallization and convection in binary systems. The model has been validated by comparison of simulations with laboratory experiments for both single-component and binary-component systems (e.g., Bennon and Incropera, 1987a, 1987b; Christenson and Incropera, 1989; Neilson and Incropera, 1991; Oldenburg and Spera, 1991, 1992a, 1992b; Yoo and Viskanta, 1992). In particular, important characteristics of solidification such as remelting of earlier formed solid, the spatial irregularity of the liquidus isotherm, the spontaneous development of high-permeability regions (i.e., channels) within mush, and the development of macroscopic compositional zonation (macrosegregation) in the solidified products are faithfully captured by the model.

## Assumptions and limitations

The most fundamental assumption invoked is that of local thermodynamic equilibrium. Equal phase temperatures and chemical potentials for components in coexisting solid and melt phases are assumed to be valid locally. Phase relations are uniquely determined by the equilibrium phase diagram. When equal temperatures and equal chemical potentials are assumed, then temperature, melt composition, and solid fraction are related to the mixture enthalpy and composition through the phase diagram and to the thermodynamic properties of relevant phases. In the present case, simple thermodynamic relations applicable to binary eutectic systems provide the means of relating temperature, enthalpy, and the compositions and amounts of all phases in each, arbitrarily small, portion of the magma body (control volume). Because solid-state diffusivities are tiny relative to those in melts, it is assumed that diffusion in the solid is negligible in comparison with diffusion in the melt (i.e., $D_s \ll D_l$) (Voller et al., 1990; Rappaz and Voller, 1990). Because of the extremely slow nature of solid-state diffusion it is unlikely that, on the scale of a single crystal (millimeter to centimeter size), perfect equilibrium will prevail, especially in rapidly chilled systems. Although it is possible to relax the assumption of local equilibrium and incorporate nonequilibrium effects (e.g., allow for effects of supercooling), the lack of a comprehensive set of experimental data for crystal nucleation and growth rates in magma makes this attempt premature, although some existent models do incorporate nonequilibrium effects associated with undercooling (e.g., Brandeis and Jaupart,

1987; Spohn et al., 1988; Kerr et al., 1989). However, none of these models accounts self-consistently for variations in melt composition and for associated changes in enthalpy, temperature, solid fraction, and magma rheological properties as in the model presented here.

It is assumed that there is no volume change upon crystallization and that solids that form are not acted upon by deviatoric stresses. Without this assumption, formation of void space could not be avoided upon solidification; additionally, the generation of internal stresses within the solid would occur during phase change. This approximation implies that density currents driven by a crystal-laden parcel of magma are ignored (i.e., constant phase densities except for variations associated with temperature and composition in the melt).

The multiphase region is viewed as a porous solid with an isotropic permeability ($K$). Although the study by Yoo and Viskanta (1992) illustrates that anisotropy of the permeability is relatively easy to incorporate into the present formulation, experimental information on the permeability anisotropy of silicate mush is nonexistent and therefore neglected.

Although restrictions are not placed on isobaric specific heat and thermal conductivities of different phases, each is assumed constant in the present version of the model (i.e., $c_s = c_l$ and $k_s = k_l$). Because the isobaric specific heat of silicate melts (l) and solids (s) are within a few percent of one another, this assumption seems reasonable. Similarly, unlike those of salt-$H_2O$ and liquid metals, the thermal conductivities of silicate liquids and solids are not appreciably different at magmatic temperatures.

Momentum transport is accomplished by Darcy percolation in solid-dominated mush ($f_s \geq 0.5$) and by internal viscous stresses in melt-dominated mush ($f_s < 0.5$). That is, in the melt-dominated, two-phase region, no relative motion exists between solid and melt; crystals are simply advected along with melt. In regions where $f_s \geq 0.5$, we assume that solid is static ($V_s = 0$) and melt percolates through the solid matrix-supported crystal plexus. The critical isofrac ($f_s = 0.5$) is chosen on the basis of available experimental and theoretical investigations (e.g., Arzi, 1978; van der Molen and Patterson, 1979; Marsh, 1981; Furman and Spera, 1985; Marsh, 1989; Lejeune and Richet, 1995).

In summary, the main limitations of the model are as follows: (1) it assumes local thermodynamic equilibrium; (2) the densities of solid and melt are solely dependent on temperature and composition, and solid and melt at the same temperature and composition have the same density; (3) the porous region is isotropic; (4) the calculations are conducted in a two-dimensional domain; and (5) the calculations are limited to binary-component systems with a simple eutectic topology.

## Mathematical model

The continuum conservation equations for mass, momentum, and energy may be expressed as

$$\frac{\partial}{\partial t}(\rho) + \nabla \cdot (\rho \mathbf{V}) = 0 \tag{3}$$

$$\rho_0 \frac{Du}{Dt} = -\frac{\partial P}{\partial x} + \nabla \cdot (\eta \nabla u) - \frac{\eta}{K}(u - u_s) \tag{4}$$

$$\rho_0 \frac{Dv}{Dt} = -\frac{\partial P}{\partial y} + \nabla \cdot (\eta \nabla v) - \frac{\eta}{k}(v - v_s) - \rho g \tag{5}$$

$$\frac{Dh}{Dt} = \nabla \cdot (\kappa \nabla h) + \nabla \cdot [\kappa \nabla (h_s - h)]$$
$$- \nabla \cdot [(h_l - h)(\mathbf{V} - \mathbf{V}_s)] \tag{6}$$

$$\frac{DC}{Dt} = \nabla \cdot (D \nabla C) + \nabla \cdot [D \nabla (C_l - C)]$$
$$- \nabla \cdot [(C_l - C)(\mathbf{V} - \mathbf{V}_s)] \tag{7}$$

where all symbols are as defined in the Appendix Table. The Boussinesq equation of state is employed so that the melt density obeys the relation

$$\rho = \rho_r [1 - \alpha(T - T_{sol}) - \beta(C_l - C_0)] \tag{8}$$

where $\rho_r$ is the density of melt of bulk composition at the eutectic temperature, and $C_l$ is the mass fraction of $KAlSi_2O_6$ in the liquid. The domain and boundary conditions and phase relations are depicted in Figures 1 and 2 as is the initial state in temperature-composition space. At the beginning of the simulation, the melt is homogeneous, isothermal, and superheated about 40 °C above the liquidus temperature of 1356 °C. Note that lines of constant melt density slope away from the $KAlSi_2O_6$ side of the diagram. As diopside crystals are extracted from melt, the density of residual liquid decreases along the liquidus as the melt composition moves toward the eutectic at $C_{sol} = 0.38$. All the simulations reported here were accomplished using bulk compositions on the diopside-rich side of the phase diagram.

The mixture continuum properties (velocity, enthalpy, composition, density, and chemical diffusivity) are defined as

$$\phi = f_s \phi_s + (1 - f_s) \phi_l \tag{9}$$

where $\phi$ is a general field variable that could be $u, v, h, C,$ or $D$. Note that the symbol $C$ denotes the mass fraction of leucite component in the mixture, and $C_l$ denotes the corresponding quantity in the liquid phase.

The hybrid formalism of Oldenburg and Spera (1992a) is used to account for momentum transport. That is, permeability and viscosity terms in the momentum equation are switched on depending on the local value of the solid fraction ($f_s$). For $f_s < 0.5$, where melt is the connected phase, no relative motion between melt and solid is allowed. In this case, the viscosity of the mixture depends on the local value of $f_s$ (e.g., see Metzner, 1985, for a review). In regions where $f_s \geq 0.5$, the only relevant viscosity is that of the liquid, and the local permeability is assumed to vary with $f_s$ according to the Kozeny-Carman expression
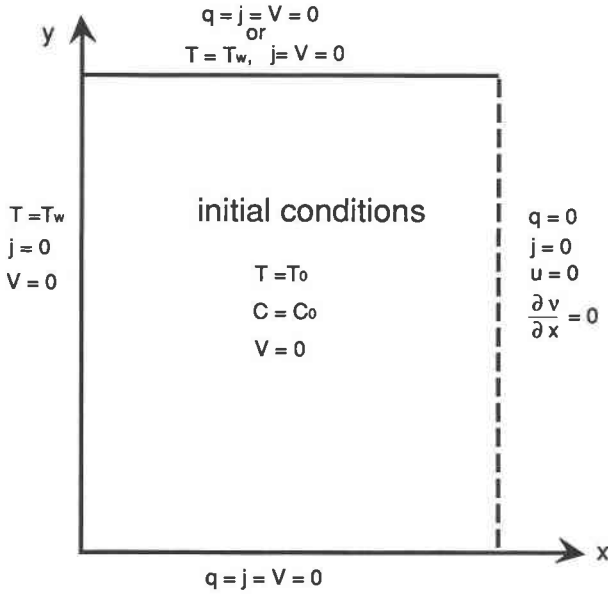
Fig. 1. Domain, initial, and boundary conditions for the simulations. The physical domain is either $4 \times 1$, $2 \times 1$, or $1 \times 1$ to simulate dikelike, boxlike, or sill-like magma bodies, respectively. The aspect ratio of the body is defined $AR = d/L$, where $d$ is the depth and $L$ the width of the body. In all cases the right side of the computational domain is a mirror plane (i.e., the midpoint of a magma body). The left side is a rigid wall set at a fixed temperature either 20 or 100 °C below the eutectic temperature with the flux of light component and the velocity equal to zero. Along the upper boundary (roof), either conditions are identical to those set along the left wall (i.e., $T_w$ = subsolidus temperature) or an adiabatic ($q = 0$) condition is imposed. The bottom boundary is adiabatic ($q = 0$), impermeable ($j = 0$), and rigid ($V = 0$). At $t = 0$, magma within the domain is isothermal ($T = T_0$), isocompositional ($C = C_0$), motionless ($V = 0$), and superliquidus (i.e., $f_s = 0$). Boundary conditions are held constant to simulate the cooling of initially homogeneous, isothermal superliquidus magma (melt) undergoing solidification.

$$K = K_0 \frac{(1 - f_s)^3}{f_s^2}. \qquad (10)$$

$K_0$ is a constant that provides a scale for the relative permeability of the two-phase region for $0.5 \le f_s < 1.0$, where relative motion between crystal and melt is allowed. Although variations in melt viscosity as a function of temperature and composition are simple to account for, these variations are extremely small in comparison with the huge variations that occur in the two-phase mixture in the solidus to liquidus interval. Consequently, the viscosity of melt is treated as a constant ($\eta_0$).

To obtain closure of the system of equations, relations are needed to relate enthalpy to temperature for solid and liquid phases, temperature to the fraction solid, and the composition and abundance of all phases to the enthalpy of the mixture. For a binary eutectic system with Ca-MgSi$_2$O$_6$ on the liquidus characterized by a single specific
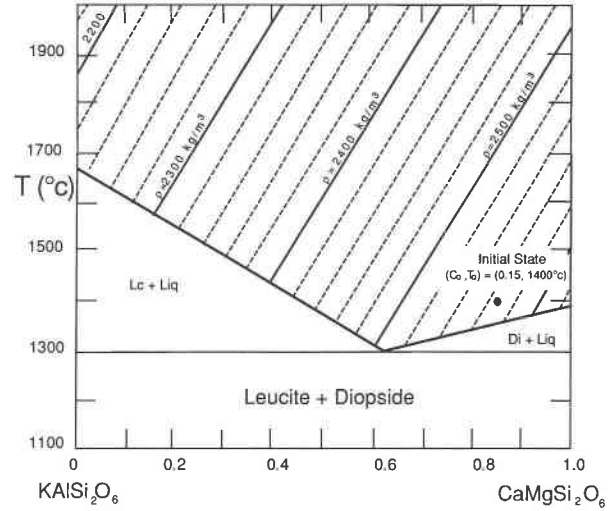
Fig. 2. Equilibrium phase relations for the system KAlSi$_2$O$_6$-CaMgSi$_2$O$_6$ after Schairer and Bowen (1938). Densities of superliquidus melts were computed from Lange and Carmichael (1990). All simulations presented in this study have initial conditions for temperature ($T_0$) and mixture composition ($C_0$) indicated on the diagram. Note that diopside is the liquidus phase and that residual melts become less dense (more K-rich) along the liquid line of descent. Lc = leucite, Di = diopside.

heat (i.e., $c_s = c_l$), the expressions for the solid, liquid, and mixture enthalpies are given respectively by

$$h_s = cT \qquad \text{for} \qquad 0 < T \le T_{liq} \qquad (11)$$

$$h_1 = cT_{sol} + \left[ 1 - \left( \frac{T_{sol} - T_{liq}}{T_{sol} - T_m} \right) \right] h_f^* + \left( \frac{T_{sol} - T_{liq}}{T_{sol} - T_m} \right) h_{f,di}$$
$$+ c(T - T_{sol}) \qquad \text{for} \qquad T \ge T_{sol} \qquad (12)$$

and

$$h = f_s h_s + (1 - f_s) h_l \qquad (13)$$

where $h$ is the mixture enthalpy, the subscripts s and l refer to solid and liquid (or melt), respectively, and the subscripts sol and m refer to the temperature of the solidus (eutectic) and fusion temperature of diopside, respectively.

The origin of the terms in Equation 12 is made clear by reference to the enthalpy-temperature diagram of Figure 3. At subsolidus ($f_s = 1$, $T < T_{sol}$) and hyperliquidus ($f_s = 0$, $T > T_{liq}$) conditions, where only solid or melt exists, the mixture enthalpy is linearly related to temperature according to

$$h = cT \qquad (14)$$

and

$$h = cT_{sol} + \left[ 1 - \left( \frac{T_{sol} - T_{liq}}{T_{sol} - T_m} \right) \right] h_f^*$$
$$+ \left( \frac{T_{sol} - T_{liq}}{T_{sol} - T_m} \right) h_{f,di} + c(T - T_{sol}) \qquad (15)$$
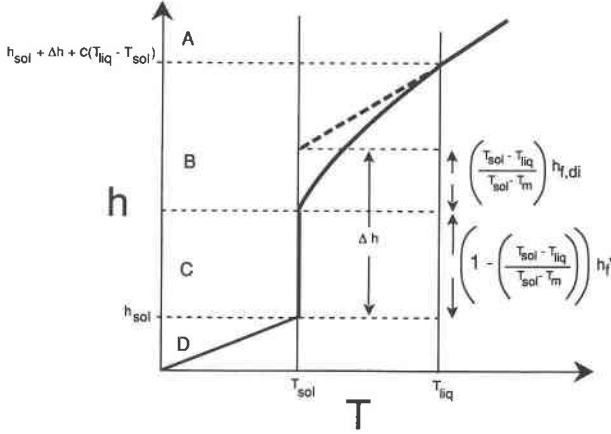
**Fig. 3.** Generalized enthalpy-temperature diagram for binary eutectic systems. The amount of melt formed at the solidus depends upon the bulk composition, as reflected by the liquidus temperature, $T_{\text{liq}}$, and the fusion enthalpies for leucite and diopside. The $h_f^*$ is the heat of fusion of solid of eutectic composition ($C_{\text{sol}} = 0.38$). The enthalpy term denoted $\Delta h$ is a fictive quantity that corresponds to the heat needed to transform solid of bulk composition ($C = C_0$) at temperature $T_{\text{sol}}$ to liquid of the same composition and temperature. The enthalpy of the two-phase mixture at the boundary between regions B and C depends on $T_{\text{liq}}$, a function only of the bulk composition under isobaric conditions.

respectively. The $h_f^*$ represents the enthalpy of fusion for diopside-leucite mixture of eutectic composition ($C_{\text{sol}}$). For the system KAlSi$_2$O$_6$-CaMgSi$_2$O$_6$, this quantity is approximately defined by $h_f^* = 0.38h_{\text{f,lc}} + 0.62h_{\text{f,di}}$ because eutectic liquid has a mass fraction of KAlSi$_2$O$_6$ of 0.38 (see Fig. 2). That is, $h_f^*$ is a eutectic-weighted linear combination of fusion enthalpies for leucite and diopside.

In region B of Figure 3, the lever rule implies that

$$f_s = \frac{T - T_{\text{liq}}}{T - T_m} \qquad (16)$$

for $f_s$ in the range $0 < f_s < [(T_{\text{sol}} - T_{\text{liq}})/(T_{\text{sol}} - T_m)]$. This expression may be inverted to give an explicit relationship between temperature and fraction solid:

$$T = \frac{T_{\text{liq}} - f_s T_m}{1 - f_s}, \qquad T_{\text{sol}} < T < T_{\text{liq}}. \qquad (17)$$

**TABLE 1.** Thermodynamic properties of diopside and leucite used in the simulations

| Property | Diopside | Leucite |
|---|---|---|
| $T_m$ (K) | 1665 | 1942 |
| $T_{\text{sol}}$ (K) | 1573 | 1573 |
| $h_f$ ($10^5$ J/kg) | 3.574 | 1.642 |
| $\rho_l$ (at $T_m$)(kg/m$^3$) | 2624 | 2236 |
| $c$ [J/(kg·K)] | 1100 | 1100 |

*Note:* The fusion enthalpy for leucite was approximated using the depression of the freezing point of pure KAlSi$_2$O$_6$ at $10^5$ Pa and standard thermochemical relations based on the experimental phase diagram (Schairer and Bowen, 1938). In fact, leucite does not melt congruently.

**TABLE 2.** Relations among fraction solid ($f_s$), enthalpy ($h$), and temperature ($T$) for binary eutectic systems

| Region | $f_s$ | $T$ |
|---|---|---|
| A | 0 | $\dfrac{h - \Delta h}{c}$ |
| B | root of Eq. 17 | $\dfrac{T_{\text{liq}} - T_m f_s}{1 - f_s}$ |
| C | $(h_f^* + h_{\text{sol}} - h)/h_f^*$ | $T_{\text{sol}}$ |
| D | 1 | $\dfrac{h}{c}$ |

*Note:* Regions are depicted in Fig. 3. Additional definitions are given in the Appendix.

Substitution of Equations 11, 12, and 17, into 13 gives a quadratic expression for the mixture enthalpy as a function of $f_s$ valid within region B as shown in Figure 3:

$$h = \left(\frac{A}{1 - f_s}\right)f_s^2 - \left(\frac{2A + cT_m}{1 - f_s}\right)f_s + \frac{cT_{\text{liq}} + A}{1 - f_s} \qquad (18)$$

where

$$\Delta h \equiv A = \left[1 - \left(\frac{T_{\text{sol}} - T_{\text{liq}}}{T_{\text{sol}} - T_m}\right)\right]h_f^* + \left(\frac{T_{\text{sol}} - T_{\text{liq}}}{T_{\text{sol}} - T_m}\right)h_{\text{f,di}}. \qquad (19)$$

Note that the quantity of $\Delta h$ depends implicitly on the initial composition of the system ($C_0$) because the liquidus temperature ($T_{\text{liq}}$) depends on composition. Mixing enthalpies are almost certainly a small fraction of fusion enthalpies in this system. Therefore, ideal mixing between KAlSi$_2$O$_6$ and CaMgSi$_2$O$_6$ liquids has been assumed. Newton-Raphson iteration of Equation 18 is used to determine $f_s$ with the mixture enthalpy ($h$). Temperature, $T$, is found from Equation 17.

Finally, at the solidus temperature (region C, Fig. 3), the fraction solid ($f_s$) varies continuously in the range

$$\frac{T_{\text{liq}} - T_{\text{sol}}}{T_m - T_{\text{sol}}} \le f_s < 1, \qquad T = T_{\text{sol}} \qquad (20)$$

and the enthalpy-$f_s$ relationship is

$$f_s = 1 - \left(\frac{h - h_{\text{sol}}}{h_f^*}\right). \qquad (21)$$

Thermodynamic properties of leucite and diopside used in the calculations are listed in Table 1. The relations between $f_s$ and $h$ are summarized in Table 2.

## Methodology

To facilitate solution of the coupled partial differential equations and the supplementary relations, a nondimensionalization was performed. The dimensionless variables and the final form of the conservation expressions are presented in the Appendix. A few other details are also presented in the Appendix to define the model.

The physical significance of the dimensionless parameters of this problem must be interpreted with care and

not confused with their classical interpretation. For example, in a single-phase fluid with simple boundary conditions and no phase change, the melt convective velocity is a simple function of a dimensionless group known as the Rayleigh number, $Ra$, a measure of the importance of thermal buoyancy forces relative to the impeding effects of viscous drag. In the present problem, the irregular time-dependent configuration of the solid, melt, and mushy regions and the dependence of the fluid enthalpy on temperature, solid fraction, and composition precludes the establishment of a single set of simple (universal) scales for length, temperature, and composition. The requirement of thermodynamic equilibrium and the use of a phase diagram for the system precludes a straightforward analysis such as that commonly done in simpler problems (e.g., Trial and Spera, 1990). For example, in the two-phase region the thermally and compositionally driven flows are not independent but instead are linked through the phase diagram and the thermochemical properties of the appropriate phases. In the mush region, the ratio of chemical to thermal buoyancy depends on the slope of the liquidus curve. However, in the all-liquid region, the buoyancy ratio is not explicitly fixed by phase relations. Because of these complexities, it is not particularly useful to discuss the evolution of the system in terms of simple classical dimensionless numbers. In fact, such a simple analysis would be misleading. This is not to say that systematic relationships do not exist between field variables and the parameters of the problem, but only that these relations are not simple functions of a single dimensionless parameter. By performing a sufficient number of numerical simulations one may develop insight into the phenomena and parameters that are most important during the evolution of magma solidification in this model system.

It must be emphasized that the present model describes some very complicated processes. The phenomena described by the model may occur over the entire range of macroscopic length scales. These can be as small as crystals (millimeters to centimeters) or as large as linear dimensions of magma bodies (meters to kilometers). Solution of the equations describing the process of convective heat and mass transport becomes computationally more difficult as the length scale of the system becomes larger. Such calculations of convection are limited to values of the Rayleigh number that are small relative to those of natural magma bodies. Except for the length scale, all the parameters in $Ra$ are fixed in terrestrial systems by the choice of the components of the phase diagram and the general range of temperatures of the system. Employing the correct thermophysical parameters for the leucite-diopside binary system in $Ra$, we find the length scale $L$ to be on the order of centimeters even for the largest values of $Ra$ for which calculations can be performed. This limitation to small systems should not be seen as a serious defect. In fact, the model describes processes that would occur at larger length scales and larger values of $Ra$. Furthermore, the crucial coupling between the processes is

described, and this coupling is part of any phase-change system, regardless of length scale.

Each conservation equation can be cast into a general form consisting of an unsteady term, an advective term, diffusion-like terms, and generalized source terms (Oldenburg and Spera, 1990). Once in this general form, the equations are amenable to solution by a primitive variable, control-volume based, iterative finite-difference algorithm. Details of the implementation used are presented in Oldenburg and Spera (1990, 1991, 1992a, 1992b).

## RESULTS

### Introduction

Solidification of melt in the binary system $KAlSi_2O_6$-$CaMgSi_2O_6$ was simulated for variously shaped, two-dimensional domains with boundary and initial conditions as depicted in Figure 1. In all cases the temperature along the left side is set at some constant value below that of the solidus (eutectic) temperature ($T_{sol}$) to simulate a cold wall (i.e., $T_w = T_{sol} - X$, where $X = 20$ or $100$ °C). The upper boundary is either adiabatic or set at the same subsolidus temperature as the left wall. All boundaries are rigid ($V = 0$) and impermeable except the midplane of the domain, which is a mirror plane, with appropriate boundary conditions. The computation is performed in one-half of the physical domain (i.e., the magma chamber per se) taking advantage of the symmetry of the problem. The results presented here are portrayed in one-half of the physical domain. A few cases were computed for the entire domain, and the solution was found to be essentially symmetric for all field variables.

By far, the most informative method of analysis is by examination of two-dimensional animations depicting the temporal evolution of field variables such as the bulk composition ($C$), melt composition ($C_l$), temperature ($T$), fraction solid ($f_s$), mixture enthalpy ($h$), and the flow field ($V$). Animation has revealed the dynamic and unsteady nature of convective solidification, including the development of heterogeneity in both melt composition and the fraction solid, the nonmonotonic behavior of the kinetic energy (velocity) of magma, and the variation of heat extraction rates through time. Complex, time-dependent flow structures develop during solidification because of the strong effects of compositional buoyancy in the system modeled ($R\rho \approx 3$). Results of this study are portrayed here by use of time-series plots of spatially averaged quantities and freeze-frame snapshots of particular field variables. Video animations portraying the evolution of all field variables are available and provide a very informative view of the evolution of convective solidification.

In the next section, a detailed description of a typical simulation is given. This is followed by a discussion of the sensitivity of system behavior on (1) magma-body shape, (2) location of cooling surfaces (i.e., marginal cooling or simultaneous marginal and roof cooling), and (3) the solidification rate. Then the results are shown at an
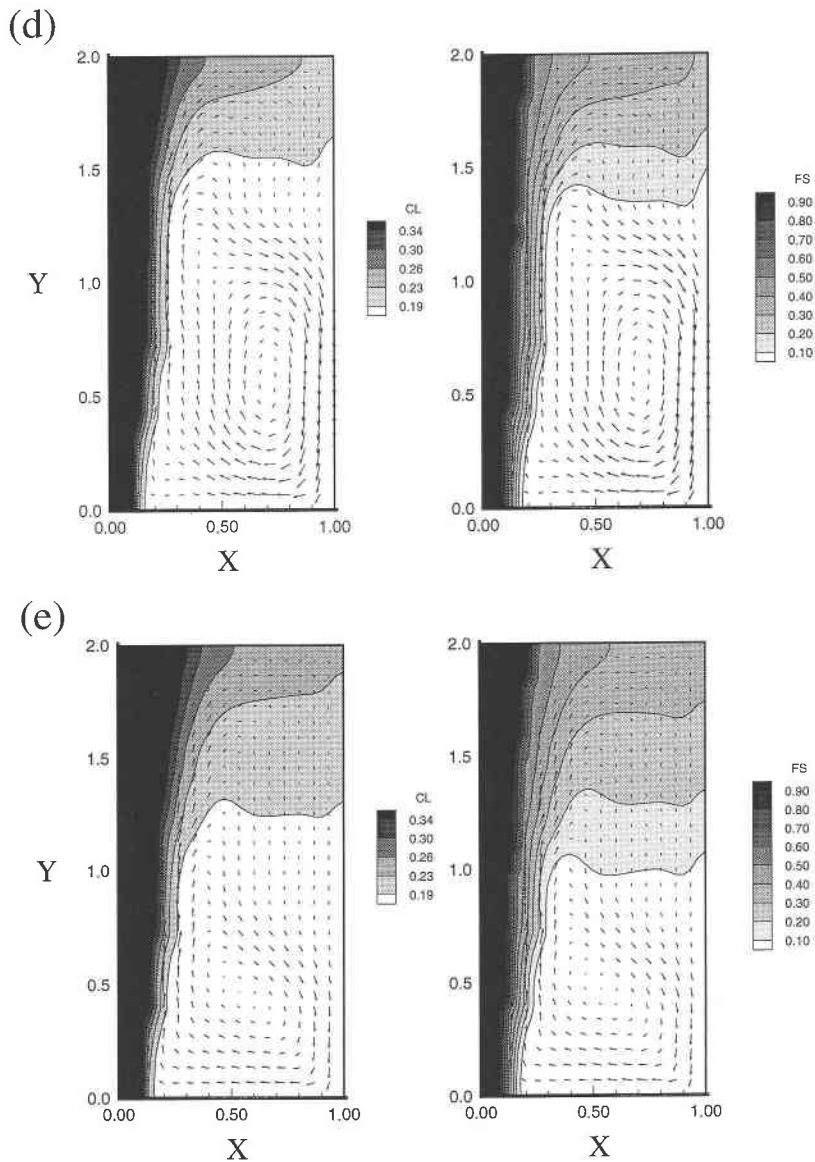
(d)



(e)
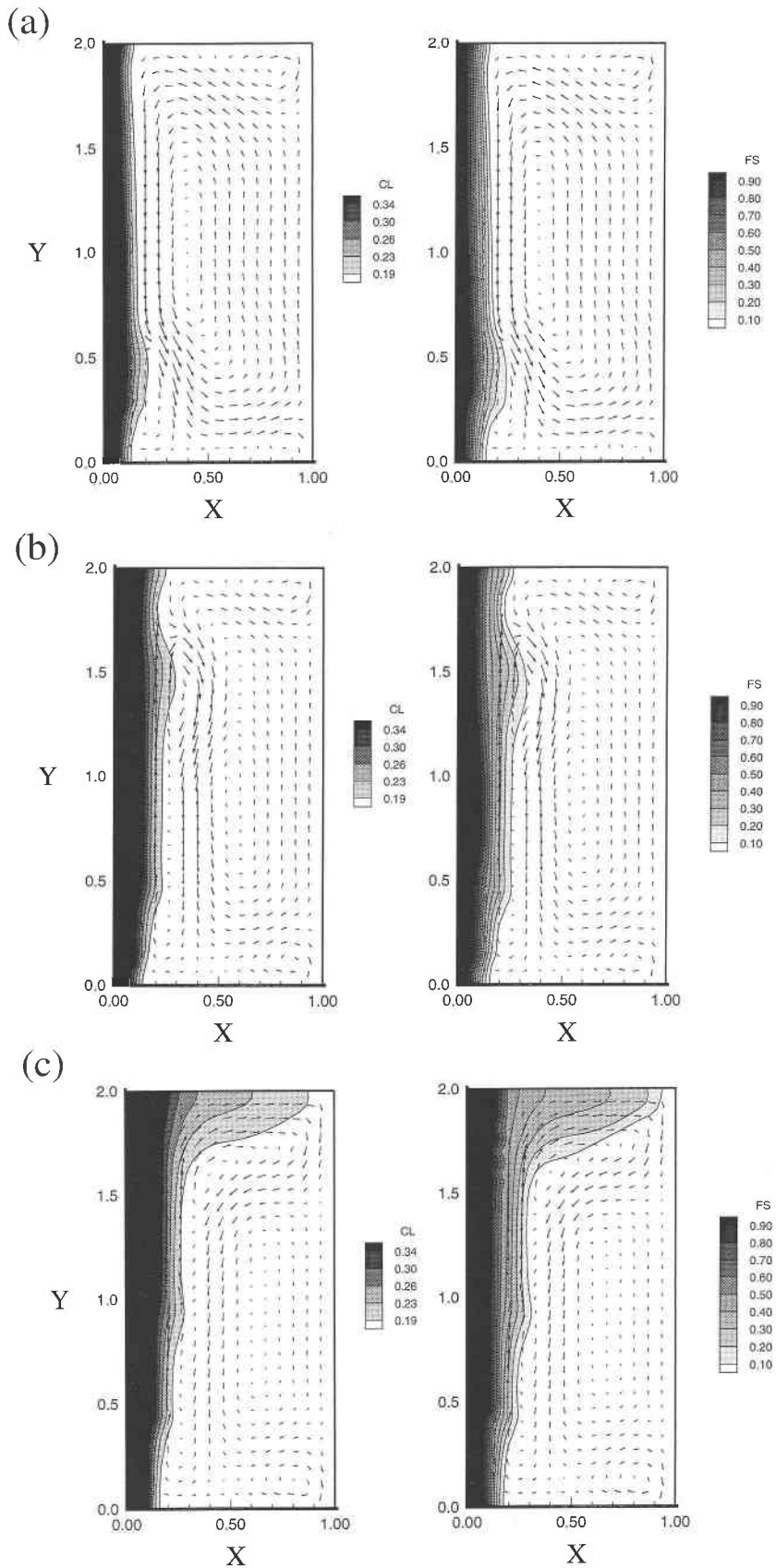


Fig. 4. Development of flow field ($V$), liquid composition ($C_l$), and fraction solid ($f_s$) for solidification of magma from a vertical sidewall in a boxlike domain. Note that $C_l$ was not normalized; it represents the mass fraction of $KAlSi_2O_6$ component in the liquid phase. Roof and bottom boundaries are adiabatic and rigid. Left margin simulates a cold country rock–magma contact at temperature $T_w = T_{sol} - 100$ °C, where $T_{sol}$ is the eutectic temperature in the system $KAlSi_2O_6$-$CaMgSi_2O_6$. The flow field for the mixture velocity is shown by nondimensional maximum mixture-velocity vectors. Note how the mush thickens with time through the sequence **a–e**. (**a**) Nondimensional time $\bar{t} = 0.01$. At $\bar{t} = 0.01$, the effects of crystallization-induced buoyancy are important at the left bottom corner of the magma body, where $KAlSi_2O_6$-enriched melt is in clockwise circulation. Solid lines are isocomps. (**b**) Nondimensional time $\bar{t} = 0.02$. Note the enhanced development of clockwise flow in the mushy region along the solidification front, where $KAlSi_2O_6$-enriched melt forms by fractionation. In melt-dominated regions ($f_s \approx 0$), the circulation remains counterclockwise. Note existence of eu-tectic melt-enriched porosity waves that travel vertically. These are especially striking in two-dimensional animation and represent an interesting phenomenon in porous media geochemical dynamics. Evolved melt is delivered episodically (but continuously) to the top of the magma body by porosity-wave transport. (**c**) Nondimensional time $\bar{t} = 0.03$. Isocomps and isofracs as in **b**. Note strong development of countercurrent flow with leucite-enriched melt accumulating roofward to form a compositionally zoned region within a roofward-thickened mushy region. (**d**) Nondimensional time $\bar{t} = 0.04$. Isocomps and isofracs as in **b**. Flow is strongly defined by clockwise rotation resulting from buoyancy torque associated with generation of chemical buoyancy within the mush along the left sidewall. The roofward mushy zone is stratified in $KAlSi_2O_6$ component in the upper central part of the magma body. (**e**) Nondimensional time $\bar{t} = 0.05$. Isocomps and isofracs as in **b**. About 30% of the magma body has solidified by this time. The magma body is vertically stratified with respect to melt composition, temperature, and phenocryst content (i.e., fraction solid).

**TABLE 3.** Parameters held constant and applicable for all simulations reported upon in this study

| | | |
|---|---|---|
| $C_0 = 0.15$ | $C_{sol} = 0.38$ | $T_{liq} = 1356\ °C$ |
| $T_0 = 1400\ °C$ | $T_{sol} = 1300\ °C$ | $h_f^* = 2.84 \times 10^5\ J/kg$ |
| $\Delta h = 3.28 \times 10^5\ J/kg$ | $\alpha = 5 \times 10^{-5}\ K^{-1}$ | $\eta_0 = 5\ kg/(m \cdot s)$ |
| $\kappa = 10^{-6}\ m^2/s$ | $\beta = 0.07$ | $Da = 5.3 \times 10^{-8}$ |
| $Pr = 1946$ | $Ra = 1.52 \times 10^5$ | $Rs = 4.67 \times 10^5$ |
| $St = 0.338$ | $R\rho \equiv Rs/Ra = 3.2$ | |

*Note:* Additional thermodynamic properties are given in Table 1.

advanced time when most of the magma has crystallized, depicting the extent of mineralogical zonation within the crystallized magma body.

**Simulation overview**

A typical result is discussed here for crystallization within a boxlike magma body. To focus on the sidewall processes, the roof and floor of the body are adiabatic (see Fig. 1) and the left margin is a vertical magma–country rock wall along which the temperature is fixed at 100 °C below that of the eutectic temperature in the system $KAlSi_2O_6$-$CaMgSi_2O_6$. Note that the computational domain is one-half of the cross-sectional area of the two-dimensional magma body. Parameters used to define the model are collected in Table 3. Figure 4 shows the development of the velocity, liquid composition, and solid fraction fields at nondimensional times $0.01 \leq \bar{t} \leq 0.05$ in increments of 0.01. Recall (see the Appendix) that real time ($t$) is related to nondimensional time ($\bar{t}$) by $t = \bar{t}L^2\Delta h/\kappa c(T_0 - T_{sol})$ or $t = \tau\bar{t}$, where $\tau$ is a characteristic scale for time for this problem. Note that the initial temperature ($T_0$), the solidus (or eutectic) temperature ($T_{sol}$), and the characteristic fusion enthalpy (see Eq. 19) are all factors. Systems initially close to their solidus (small superheat) and with large fusion enthalpies evolve less rapidly than those with larger amounts of superheat. For the particular model system studied here, a nondimensional time of 0.01 corresponds roughly to 120 yr and 3000 yr for bodies of 1 and 5 km thickness, respectively.

For a magma-body thickness of 3 km the time interval between successive snapshots is about $10^3$ yr. During this time interval (Fig. 4a–4e), about 30% of the magma, initially superheated by 40 °C, crystallizes. In Figure 5, time-series plots that depict the variation of the maximum mixture velocity ($\bar{V}_{max}$) and spatially averaged fraction solid ($f_{s,av}$) are shown for the evolution portrayed in Figure 4.

At the very earliest times ($\bar{t} < 0.01$, not shown), the cold left wall sets up a descending (counterclockwise) thermally driven flow throughout the entire domain. Melt velocities reach their greatest values ($\bar{V}_{max} \approx 250$) at very early times (Fig. 5), at which the maximum value for $\bar{V}_{max}$ is close to the value predicted using the scale relation given by Trial and Spera (1990) for a thermally driven single-phase flow:

$$\bar{V}_{max} \approx \tfrac{3}{5}Ra^{1/2}. \qquad (22)$$

This velocity corresponds to a dimensional velocity of

about 10 m/yr based on a magma-body thickness of 1 km and the parameters given in Table 3. For comparison, the Stokes settling rate of a 2 mm diameter spherical olivine crystal is about 1 m/yr.

At $\bar{t} = 0.01$ (Fig. 4a), a counterflow with a clockwise sense of rotation nucleates near the left bottom corner of the magma body as crystallization of diopside enriches residual melt in low-density leucite component. This sets up a chemically driven flow that deflects the isocomps; a region of enriched mush moves upward as a porosity wave (cf. Fig. 4a–4c). At $\bar{t} = 0.01$, the flow is dominated by thermal effects throughout most of the domain, except near the crystallization front where chemical buoyancy is being vigorously generated. Note the development of small clockwise vortices at the top and bottom of the magma body along the mirror plane (right side).

At later times (Fig. 4b and 4c), the thickened mushy region begins to dominate the flow along the solid-mush and mush-liquid transition regions. Although flow within the liquid portion ($f_s = 0$) is still thermally driven, an increasingly smaller (but still dominant) region of the domain is affected. At $\bar{t} = 0.02$, $\bar{V}_{max}$ is two to three times smaller than the peak $\bar{V}_{max}$, and $\bar{V}_{max}$ is again smaller at $\bar{t} = 0.03$. At $\bar{t} = 0.03$, about 20% of the magma has crystallized. Notice by comparing Figure 4b and 4c that a large amount of $KAlSi_2O_6$-rich liquid is delivered to the top of the magma reservoir when the porosity wave that contains melt of eutectic composition ($C_l = 0.38$) reaches the roof. This causes the incipient development of a stratified region at the top of the magma body. Note also that the isofracs (lines of constant fraction solid) within the mush remain subparallel to the $C_l$ isocomps, an effect that reflects the attainment of local thermodynamic equilibrium within the mushy two-phase region.

At $\bar{t} = 0.05$ (Fig. 4e), about 30% of the magma has crystallized (Fig. 5). Stratification of $f_s$ and $C_l$ is well developed in the middle of the magma body, especially in the upper 40% of the chamber. The flow now is essentially chemically driven because of solidification effects. Although irregular in plan, the circulation is mainly clockwise, with maximal mixture velocities along the mush-liquid interface (i.e., near the $f_s \approx 0$ isofrac).

Perhaps the most salient feature of the evolution portrayed in Figures 4 and 5 and noted in all the numerical experiments is the relationship between the development of compositionally zoned melt near the top of the magma body and the change in dynamic regime. At early times, the flow is thermally driven, and $KAlSi_2O_6$-rich melt does

not accumulate roofward. At later times, chemical buoyancy plays an increasingly important role, and melts become more evolved during the course of solidification. The transition from thermally driven to chemically driven flow occurs because of the relatively large value of $R\rho$ (~3) characteristic of this particular binary system. The buoyancy ratio $R\rho$ depends on the eutectic composition ($C_{sol}$) and temperature ($T_{sol}$), the initial conditions ($C_0$ and $T_0$), and the temperature and composition dependence of the density of $KAlSi_2O_6$-$CaMgSi_2O_6$ mixtures. As magma undergoes progressive solidification, the fractional volume of the body within the crystallization-temperature interval increases. This is noted by examination of the fraction solid ($f_s$) field plotted in Figure 4. It is in this volumetrically expanding mushy region that chemical buoyancy is generated.

In Figure 6, a sequence of snapshots is shown depicting the evolution of the temperature field superimposed on the flow field for the time interval $0.01 \leq \bar{t} \leq 0.05$. Upflow is most rapid in the melt-dominated ($f_s < 0.5$) portion of the two-phase region. The solidus isotherm remains nearly subparallel to the $f_s = 0.5$ isofrac throughout the course of solidification.

The fact that the most vigorous upflow occurs in a part of the domain where no relative motion between solid and melt exists illustrates the critical nature of the assumptions made to characterize the rheological and permeability properties of magmatic mush. This is the crux of the magma-diversity problem by convective fractionation. Additional experimental work on the rheology of magma and the relationship between permeability and fraction solid is needed for further progress. The kinetics and dynamics of the microinterface between crystals and melt and how these processes can be modeled at the macroscopic level is a challenging problem for magma dynamicists.

### Roof and sidewall cooling

A numerical experiment was performed for conditions identical to the last example except that both the sidewall and the roof were cooled to $T_{roof} = T_{wall} = T_{sol} - 100$ °C. In the previous case the roof was treated as an adiabatic surface to isolate the effects of sidewall crystallization.

The overall dynamics are broadly similar to the sidewall cooling case; as time progresses the effects of chemical buoyancy come to dominate the flow. There are some significant differences, however. Roof cooling creates additional thermal instabilities associated with cooling from above. This triggers small-scale horizontal convection, more vigorous convection early on, and, of course, higher solidification rates. This may be seen by comparison of Figures 5 and 7. Note, in particular, the higher $\bar{V}_{max}$ and its more rapid decay in the roof-cooled case, as well as the greater extent of crystallization (~45%) in comparison with the adiabatic roof case in Figures 4 and 5.

Figure 8 is a snapshot sequence for the roof and sidewall-chilled box. Frame by frame comparison of Figures 4 and 8 reveals some interesting differences. At early times
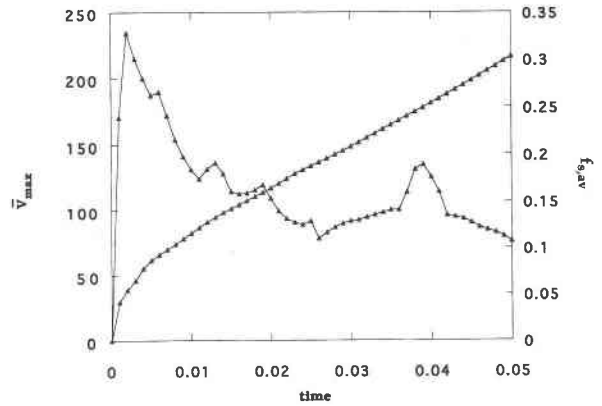


Fig. 5.  Time-series plots for the simulations illustrated in Fig. 4. The nondimensional maximum velocity ($V_{max}$) and spatially averaged fraction solid ($f_{s,av}$) are plotted against time. The nonmonotonic behavior of $V_{max}$ is correlated to qualitative variations in the flow field, as portrayed in Fig. 4. The rate of solidification ($df_s/dt$) is nearly constant for $\bar{t} > 0.01$. About 30% of the magma body has solidified at $\bar{t} = 0.05$. This corresponds roughly to 5000 yr for a 3 km thick magma chamber.

($\bar{t} < 0.01$), motion near the cooled, vertical left wall is dominated by negative thermal buoyancy (Fig. 8a). However, unlike the case for the adiabatic roof (Fig. 4a) when cooling out the top takes place, strong downwelling owing to roofward heat loss occurs (cf. Figs. 4a, 4b, 8a, 8b). At $\bar{t} = 0.02$, upward wall flow develops along the entire left sidewall, and K-rich melt accumulates under the downward-growing crystalline top. By comparing Figures 4 and 8, it is noted that thermal and compositional stratification are enhanced by cooling through the roof. At the latest time, $\bar{t} = 0.03$ (Fig. 8c), the flow is chemically driven throughout the entire domain, and the solidified roof zone is substantially thicker than that along the sidewall. Perhaps the most significant feature of this case is that, as in the adiabatic roof case, a chemically stratified mushy region develops in the upper part of the domain during convective solidification.

### Magma-body shape

Magma bodies undoubtedly come in a variety of shapes and sizes. To assess the sensitivity of magma-body shape on the evolution of solidification, a series of simulations were performed with identical initial and boundary conditions but differing shapes. Bodies with aspect ratio ($AR$) equal to 2 (dike), 1 (box), and ½ (sill) were cooled from above and from the sides ($T_{roof} = T_w = T_{sol} - 20$ °C). The rate of heat extraction, which is proportional to the boundary temperature, is somewhat smaller than in the case examined in Figures 4–6, where the wall temperature was 100 °C below the eutectic temperature and the roof was taken as an adiabatic surface.

In Figure 9, the maximum convective velocity ($\bar{V}_{max}$) and the fraction solid ($f_s$) are plotted against time for a sill, dike, and box magma body. As expected, the sill
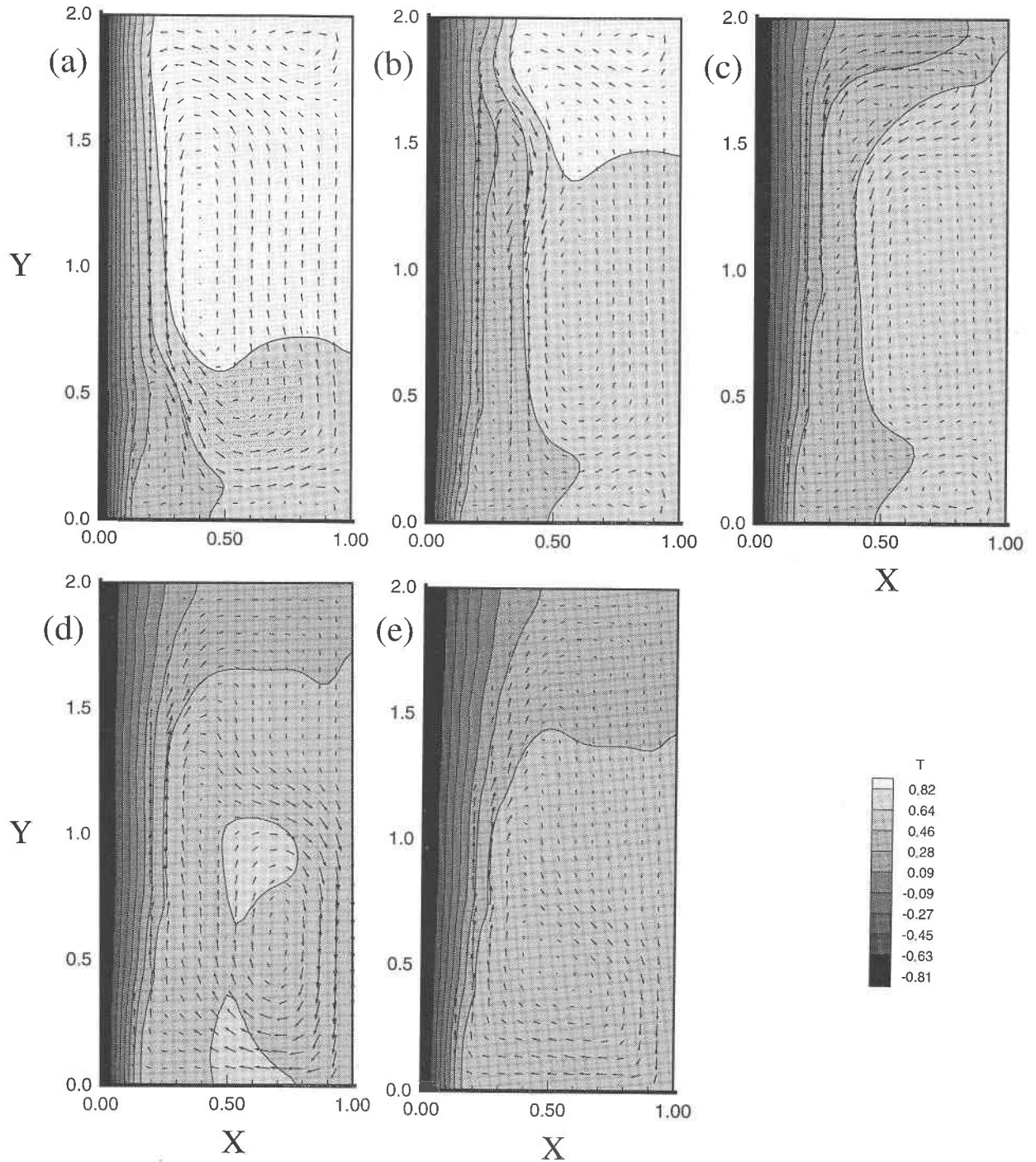
Fig. 6. Evolution of the nondimensional temperature field for the simulations presented in Figs. 4 and 5. The solidus isotherm is $\overline{T} = 0$; initially $\overline{T} = 1$ throughout the entire domain. (a) Nondimensional time $\bar{t} = 0.01$. Note nucleation of a clockwise circulation in the bottom left part of the domain. (b) Nondimensional time $\bar{t} = 0.02$. Compositional buoyancy effects overcome negative thermal buoyancy, and local upflow occurs along the entire sidewall. (c) Nondimensional time $\bar{t} = 0.03$. Evolved melt is being delivered to the top of the magma body at this time. (d) Nondimensional time $\bar{t} = 0.04$. Note development of thermal zoning within the magma body. (e) Nondimensional time $\bar{t} = 0.05$. For characteristic dimension $d = L = 3$ km, this snapshot corresponds to roughly 5000 yr after the beginning of crystallization.
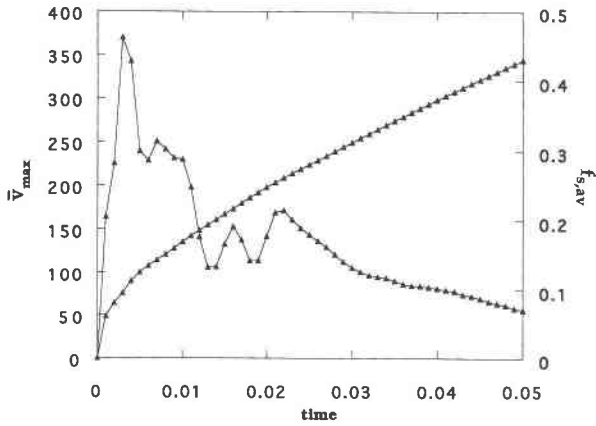
Fig. 7. Time-series plots for the simulations illustrated in Fig. 8. The nondimensional maximum velocity ($V_{max}$) and spatially averaged fraction solid ($f_{s,av}$) are plotted against time. This case is identical to that presented in Fig. 5, except that cooling takes place through the roof as well as the sides. About 45% of the body has solidified at $\bar{t} = 0.05$, which corresponds to roughly 5000 yr for a 3 km thick magma body.

cools the fastest and the dike the slowest. At $\bar{t} = 0.05$, more than 35% of the sill has solidified, whereas only about 22% of the dike has crystallized. Maximum velocities are greatest for the dike because of its vertical extent. In all cases, $\bar{V}_{max}$ is nonmonotonic, although the flow tends

to become sluggish as crystallization occurs. For a magma body of 1 km width, $\bar{V}_{max} = 100$ corresponds roughly to a convective velocity of several meters per year, which is the same as the settling rate of a millimeter-sized phenocryst. Solidification times are roughly 30, 20, and 15 ka for the sill, box, and dike, respectively ($L = 3$ km).

In Figure 10, a series of snapshots are shown for the variously shaped bodies at equal time intervals in the range $0.01 \leq \bar{t} \leq 0.05$. In each case the flow is thermally dominated at early times and becomes more chemically driven as solidification proceeds. Because the sill cools fastest, stratification develops quickly, and at $\bar{t} = 0.05$ the upper half of the sill is either completely solidified or occupied by mush that includes chemically zoned melt. For all shapes, thermal and chemical stratification becomes well developed near the roof at later times (e.g., cf. Fig. 10g, 10h, and 10i).

Careful examination of Figure 10 reveals that the tendency to form compositionally stratified melt near the top of the magma body occurs regardless of body shape. The key point is that the tendency to form a compositionally layered system is most sensitively dependent upon the thermodynamic and transport properties of the magma rather than the shape of the body per se. The main role of body shape is in controlling the rate at which compositional zonation develops as a result of the interaction between the surface area of magma body–country rock, rate of solidification, rate of generation of chemical
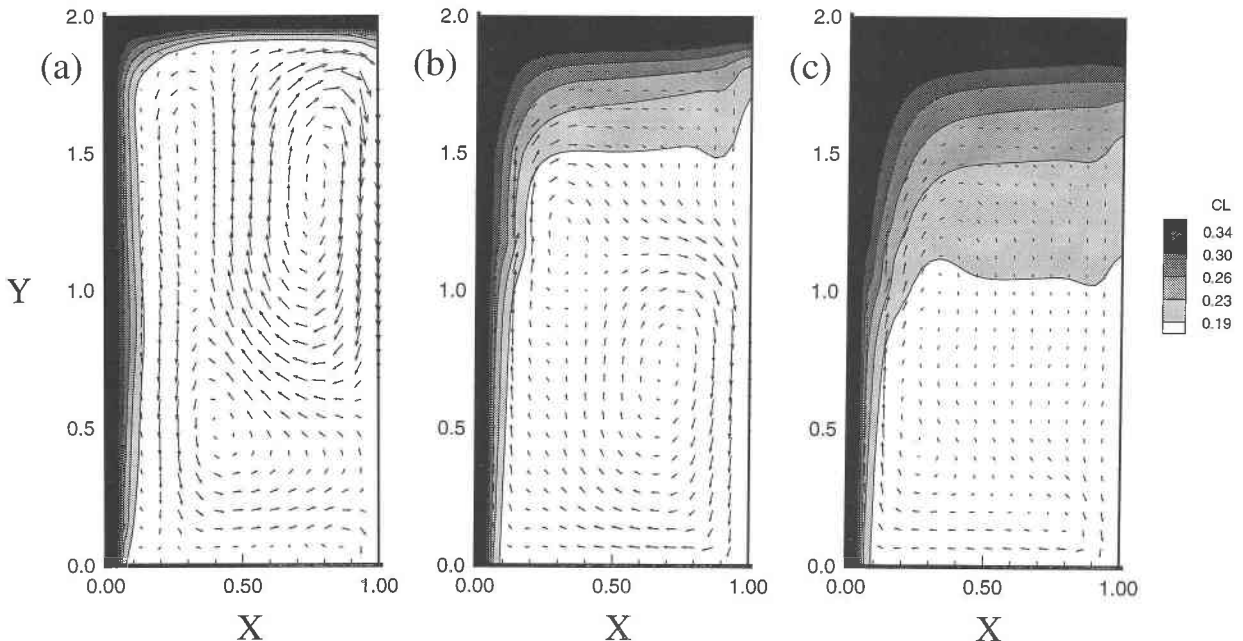


Fig. 8. Development of flow field (V) and liquid composition ($C_l$) for solidification of magma from the side and roof of a 1 × 1 magma body. Roof and left sidewall have $T_{roof} = T_w = T_{sol} - 100$ °C. Bottom boundary is rigid and adiabatic; right side is a mirror plane. Plotting symbols are identical to those described in legend to Fig. 4. (a) Nondimensional time $\bar{t} = 0.01$. In comparison with Fig. 4a, the compositionally driven flow is not as well developed along the bottom of the sidewall. Note the growth of a solidified zone along the roof. (b) Nondimensional time $\bar{t} = 0.02$. Significant upward flow extends along the entire sidewall, and the downward thickening mush is strongly zoned with respect to $KAlSi_2O_6$ component. (c) Nondimensional time $\bar{t} = 0.03$. Note the well-developed, liquid compositional stratification within the roofward mush zone.
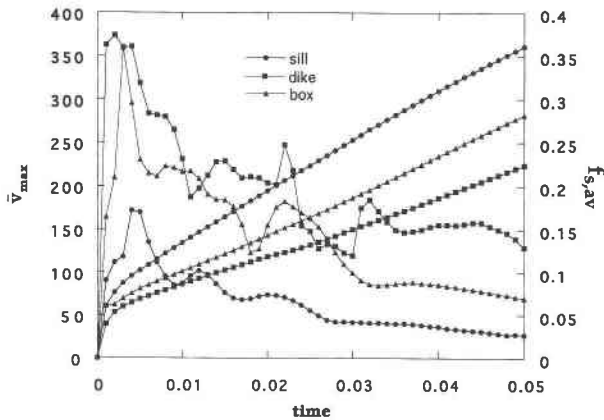
Fig. 9. $V_{max}$ and $f_{s,av}$ for dike, box, and sill magma bodies. Cooling is from the roof and sidewall ($T_{roof} = T_w = T_{sol} - 20$ °C). The curves for the box can be compared with the case illustrated in Fig. 7, which is identical except that $T_{roof} = T_w = T_{sol} - 100$ °C. Thermal buoyancy effects are maximized in the dike because of the greater extent of cooling surface. These greater thermal buoyancy forces show up as a more vigorous flow compared with the shallow enclosure (sill) solution. The faster cooling of the sill is also seen by the greater value for the spatially averaged function solidified ($f_{s,av}$) at a given time for the sill relative to the dike.

buoyancy, and generation of latent heat. These interactions are highly nonlinear and give rise to unsteady flow, including reversals in flow directions that occur during the course of solidification.

### Mineralogic zonation

Radially zoned granitic (*sensu lato*) bodies are exceedingly common in the geologic record and include both normally zoned (mafic margin, silicic core) and reversely zoned plutons (e.g., Bateman and Chapple, 1979; Ayuso, 1984). Large-volume layered intrusions are almost always vertically zoned in terms of modal abundances and bulk composition. It seems logical, if not obvious, that a connection ought to exist between zoned extrusive bodies (ignimbrites, lava flows, and domes) and plutonic bodies. To study the implications of the model presented here with respect to the origin of modally zoned intrusive bodies, a series of simulations was performed until essentially all the magma crystallized ($f_s \approx$ unity). In Figure 11, results from a typical case are shown for the spatial variation in modal leucite fraction. In this example, cooling from both the roof and sides was allowed, with $T_{roof} = T_{side} = T_{sol} - 100$ °C. The parameters of the simulation are otherwise identical to those illustrated in Figure 8.

Initially, homogeneous melt of bulk composition $C = 0.15$ fills the magma chamber. This composition corresponds to 85% by mass of $CaMgSi_2O_6$ component and 15% by mass of $KAlSi_2O_6$ component. At $\bar{t} = 0.31$, more than 90% of the melt has crystallized, and substantial variations in modal abundances are clearly present. Diopside is concentrated near the floor of the body ($C \simeq 0.14$) and is also enriched, relative to the initial composition along the left (cooled) vertical wall. In contrast, leucite is enriched in the upper part of the magma body and reaches a maximum value of about 0.17 in the middle of the body.

The mineralogic zonation established in the intrusive magma body has both a horizontal and vertical component. For example, a horizontal slice through the body just above its midpoint would reveal a radially zoned pluton. Similarly, a vertical profile taken along the right side of the domain would show a sandwich horizon of $KAlSi_2O_6$-enriched material. We emphasize that this zonation resulted from an initially homogeneous melt.

In the particular model shown in Figure 11, solidification is rapid because the boundary temperature, along both the roof and the right side, is set to $T_{sol} - 100$ °C. In other simulations with a smaller undercooling and an adiabatic roof, even greater modal variations are found because of a more protracted cooling history.

### Summary

Compositionally zoned ignimbrites and plutonic bodies are exceedingly common. In extrusive deposits, evolved magma commonly erupts early. As eruption continues, magma compositions become more mafic. In intrusive bodies, it is common to find normally zoned bodies with more evolved bulk compositions inward and more mafic compositions toward the magma–country rock contact. In regions characterized by considerable relief, bulk compositions generally become more mafic with increasing depth. When roof zones of plutons or intrusions are exposed, it is not uncommon to find sandwich horizons. These extremely well-known attributes of igneous systems can be simulated by the convective solidification model illustrated in this study. Although there are significant limitations of this model in its present form, incorporation of more accurate macroscopic physics on the basis of a deeper understanding of microscopic interfacial dynamics and extension to three dimensions and multicomponent systems is presently in sight because of significant advances in high-performance computing. At the same time, the thermochemical database for oxide and silicate phases relevant to magmatic rocks is expanding

$\longrightarrow$

Fig. 10.  Snapshots showing a comparison of the evolution of melt composition ($C_1$) and flow field (velocity vectors) for magma crystallization in a dike, box, and sill. Cooling occurs along the sidewall and roof, where the temperature is $T_{roof} = T_w = T_{sol} - 20$ °C. Note different $x$- and $y$-axis scales among the figures.

Also note the common occurrence of vertically migrating porosity waves. (a) Dike at $\bar{t} = 0.01$, (b) box at $\bar{t} = 0.01$, (c) sill at $\bar{t} = 0.01$, (d) dike at $\bar{t} = 0.03$, (e) box at $\bar{t} = 0.03$, (f) sill at $\bar{t} = 0.03$, (g) dike at $\bar{t} = 0.05$, (h) box at $\bar{t} = 0.05$, and (i) sill at $\bar{t} = 0.05$.
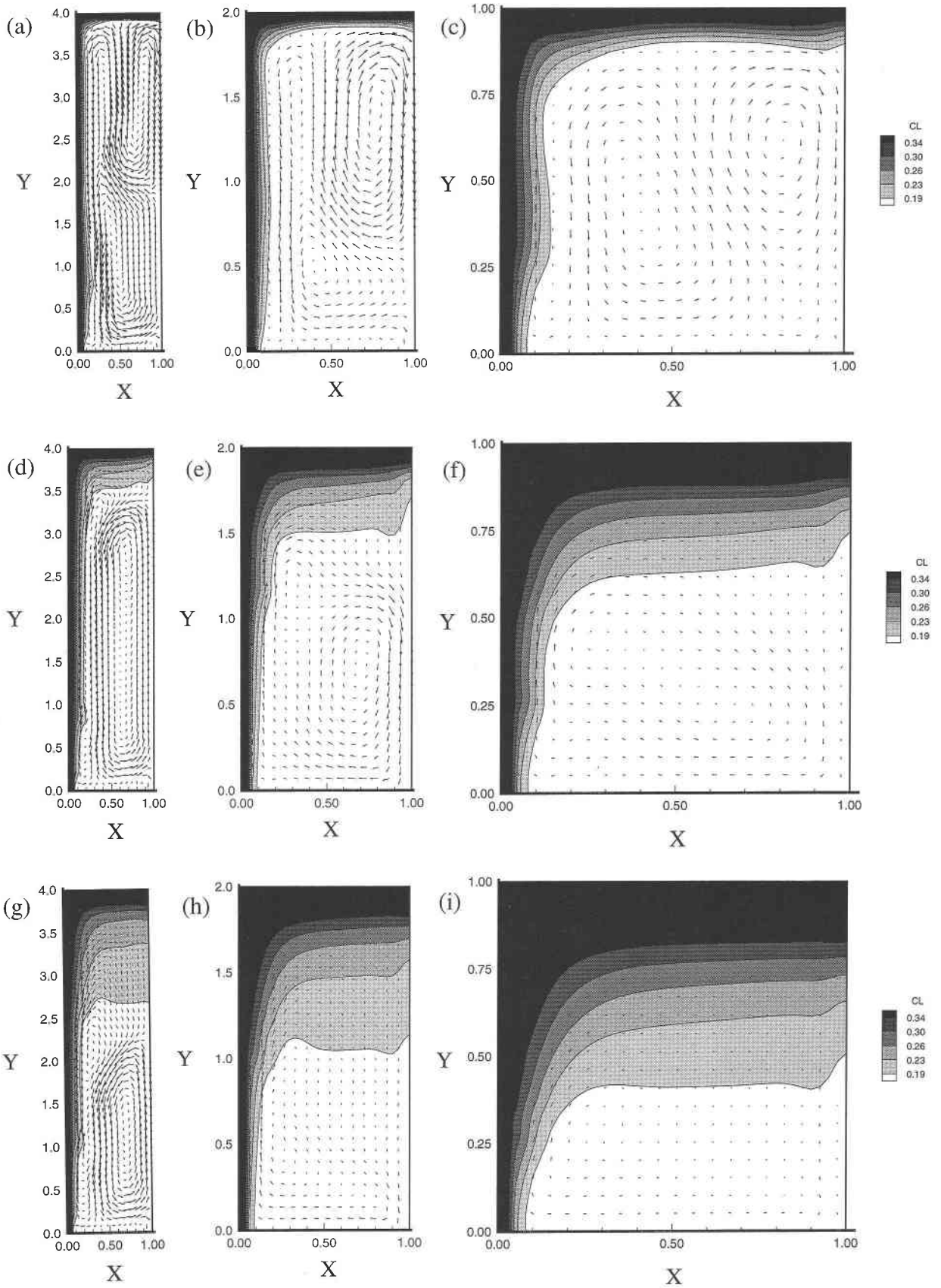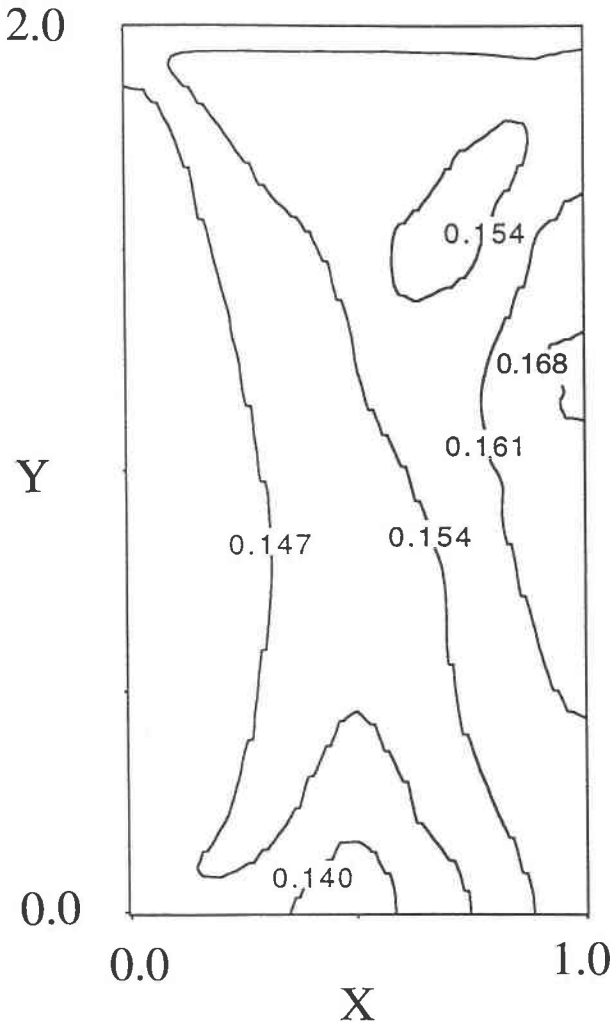
Fig. 11. Depiction of the modal amount of leucite in equant magma body ($AR = 1$) at $\bar{t} = 0.31$ when the average fraction solidified is >90%. The magma body is cooled from the right side and from the roof ($T_{\text{roof}} = T_{\text{side}} = T_{\text{sol}} - 100$ °C). Other parameters are collected in Table 3. Initially, magma is superheated by 40 °C and is homogeneous with $C = 0.15$ (i.e., 15% $KAlSi_2O_6$ component in the melt). Contours are drawn for the modal amount of solid leucite in the two-phase (diopside + leucite) mixture. Note the modal enrichment of leucite near the center of the body ($C = 0.168$). The most mafic part of the body is along the floor midway between the left sidewall and the center of the model pluton. The minimum and maximum values of $C$ are 0.135 and 0.170, respectively. Five equispaced contours are indicated. Results from a simulation identical to the one pictured but with $T_{\text{roof}} = T_{\text{side}} = T_{\text{sol}} - 20$ °C show a larger range of mineralogical modal variation. The larger range for $C_{\text{max}}-C_{\text{min}}$ at the slower solidification rate is a consequence of the assumption of local thermodynamic chemical equilibrium.

(Ghiroso et al., 1994). Igneous petrologists have good reasons to be optimistic about the chances to understand better the origin of magmatic diversity by mechanisms involving simultaneous convection and phase change. The calculations presented here do not apply to large, mafic-layered intrusions that show strong evidence of multiple intrusion and fractional crystallization. Transiently permeable magma-body floors need to be incorporated into the next generation of the simulator.

## REFERENCES CITED

Arzi, A.A. (1978) Critical phenomena in the rheology of partially melted rocks. Tectonophysics, 44, 173–184.

Ayuso, R. (1984) Field relations, crystallization, and petrology of reversely zoned granitic plutons in the Bottle Lake Complex. U.S. Geological Survey, 1320, 64 p.

Bateman, P.C., and Chapple, B.W. (1979) Crystallization, fractionation, and solidification of the Toulumme Intrusive Series, Yosemite National Park, California. Geological Society of America Bulletin, 86(5), 563–579.

Beckermann, C., and Viskanta, R. (1988) Double-diffusive convection during dendritic solidification of a binary mixture. Physiochemical Hydrodynamics, 10, 195–213.

Bennon, W.D., and Incropera, F.P. (1987a) A continuum model for momentum, heat and species transport in binary solid-liquid phase change systems: 1. Model formulation. International Journal of Heat and Mass Transfer, 80, 2161–2170.

——— (1987b) The evolution of macrosegregation in statically cast binary ingots. Metallurgical Transactions, 18B, 611–616.

Bergantz, G.W. (1992) Conjugate solidification and melting in multicomponent open and closed systems. International Journal of Heat and Mass Transfer, 35, 533–543.

Bergantz, G.W., and Lowell, R.P. (1987) The role of conjugate convection in magmatic heat and mass transfer. In D.E. Loper, Ed., Structure and dynamics of partially solidified systems, NATO ASI Series, series E, no. 125, 370–382.

Bottinga, Y., and Weill, D.F. (1972) The viscosity of magmatic silicate liquids: A model for calculation. American Journal of Science, 272, 438–475.

Bowen, N.L. (1928) The evolution of the igneous rocks, 332 p. Dover, New York.

Brandeis, G., and Jaupart, C. (1987) The kinetics of nucleation and crystal growth and scaling laws for magmatic crystallization. Contributions to Mineralogy and Petrology, 96, 24–34.

Chen, C.F., and Turner, J.S. (1980) Crystallization in a double-diffusive system. Journal of Geophysical Research, 85, 2573–2593.

Christenson, M.S., and Incropera, F.P. (1989) Solidification of an aqueous ammonium chloride solution in a rectangular cavity: I. Experimental study. International Journal of Heat and Mass Transfer, 32, 47–68.

Dunbar, N.W., and Hervig, R.L. (1992) Petrogenesis and volatile stratigraphy of the Bishop Tuff: Evidence from melt inclusion analysis. Journal of Geophysical Research, 97, 15129–15150.

Furman, T., and Spera, F.J. (1985) Co-mingling of acid and basic magma with implications for the origin of magmatic I-type xenoliths: Field and petrochemical relations of an unusual dike complex at Eagle Lake, Sequoia National Park, California, U.S.A. Journal of Volcanological and Geothermal Research, 24, 151–178.

Galer, S.J.G., and Goldstein, S.L. (1991) Early mantle differentiation and its thermal consequences. Geochimica et Cosmochimica Acta, 55, 227–239.

Ghiorso, M.S., Hirschmann, M.M., and Sack, R.O. (1994) New software models: Thermodynamics of magmatic systems. Eos, 75, 571–574.

Gibb, G.F., and Henderson, C. (1992) Convection and crystal settling in sills. Contributions to Mineralogy and Petrology, 109, 538–545.

Hervig, R.L., and Dunbar, N.W. (1992) Cause of chemical zoning in the Bishop and Bandelier magma chamber. Earth and Planetary Science Letters, 111, 97–108.

Hildreth, W. (1979) The Bishop Tuff: Evidence for the origin of compositional zonation in silicic magma chamber. In Geological Society of America Special Papers, 180, 43–75.

——— (1981) Gradients in silicic magma chambers: Implications for lithospheric magmatism. Journal of Geophysical Research, 86, 10153–10193.

Huppert, H.E. (1990) The fluid mechanics of solidification. Journal of Fluid Mechanics, 212, 209–240.

Huppert, H.E., and Sparks, R.J. (1984) Double-diffusive convection due to crystallization in magmas. Annual Review Earth and Planetary Science Letters, 12, 11–37.

Huppert, H.E., and Worster, M.G. (1992) Vigorous convective motion in magma chambers and lava lakes. In D. Yuen, Ed., Chaotic processes in geological sciences, p. 141–174. Springer-Verlag, New York.

Huppert, H.E., Sparks, R.J., Wilson, J.R., and Hallworth, M.A. (1986) Cooling and crystallization at an inclined plane. Earth and Planetary Science Letters, 79, 319–328.

Joron, J.L., Metrich, N., Rosi, M., Santacroce, R., and Sbrana, A. (1987) Chemistry and petrography. In Progetto Finalizzato Geodinamica Monografie Finali, 8, 105–174.

Kerr, R.C., Woods, A.W., Worster, M.K., and Huppert, H.E. (1989) Disequilibrium and macrosegregation during solidification of a binary melt. Nature, 340, 357–362.

Lange, R.L., and Carmichael, I.S.E. (1990) Thermodynamic properties of silicate liquids with emphasis on density, thermal expansion and compressibility. In Mineralogical Society of America Reviews in Mineralogy, 24, 24–65.

Langmuir, C.H. (1989) Geochemical consequences of in situ crystallization. Nature, 340, 199–205.

Leitch, A.M. (1989) Evolution of a binary system crystallizing in a confined region. International Journal of Heat and Mass Transfer, 32(11), 2087–2089.

Lejeune, A., and Richet, P. (1995) Rheology of crystal-bearing silicate melts: An experimental study at high viscosities. Journal of Geophysical Research, 100, 4215–4229.

Lowell, R.P. (1985) Double-diffusive convection in partially molten silicate systems: Its role during magma production and in magma chambers. Journal of Volcanological and Geothermal Research, 26, 1–24.

Lu, F., Anderson, A.T., and Davis, A.M. (1992) Melt inclusions and crystal-liquid separation in rhyolitic magma of the Bishop Tuff. Contributions to Mineralogy and Petrology, 110, 113–117.

Marsh, B.D. (1981) On the crystallinity, probability of occurrence, and rheology of lava and magma. Contributions to Mineralogy and Petrology, 78, 85–98.

——— (1989) On convective style and vigor in sheet-like magma chambers. Journal of Petrology, 30, 479–530.

Martin, D., and Nokes, R. (1989) A fluid-dynamical study of crystal settling in convecting magmas. Journal of Petrology, 30, 1471–1500.

McBirney, A.R., Baker, B.H., and Nilson, R.H. (1985) Liquid fractionation: I. Basis principles and experimental simulations. Journal of Volcanological and Geothermal Research, 24, 1–24.

Metzner, A.B. (1985) Rheology of suspensions in polymeric liquids. Journal of Rheology, 29, 739–775.

Michael, P.J. (1983) Chemical differentiation of the Bishop Tuff and other high-silica magmas through crystallization processes. Geology, 11, 31–34.

Morse, S.A. (1988) Motion of crystals, solute and heat in layered intrusions. Canadian Mineralogist, 26, 209–224.

Neilson, D.G., and Incropera, F.P. (1991) Unidirectional solidification of a binary alloy and the effects of induced fluid motion. International Journal of Heat and Mass Transfer, 34(7), 1717–1732.

Ni, J., and Beckermann, C.A. (1991) Volume-averaged two-phase model for transport phenomena during solidification. Metallurgical Transactions, 22B, 349–361.

Nilson, R.H., McBirney, A.R., and Baker, B.H. (1985) Liquid fractionation: II. Fluid dynamics and quantitative implications for magmatic systems. Journal of Volcanological and Geothermal Research, 24, 25–54.

Oldenburg, C.M., and Spera, F.J. (1990) Simulation of phase change and convection in magma bodies. In Heat Transfer in Earth Science Studies (ASME-HTD), 149, 35–42.

——— (1991) Numerical modeling of solidification and convection in a viscous pure binary eutectic system. International Journal of Heat and Mass Transfer, 34, 2107–2121.

——— (1992a) Hybrid model for solidification and convection. Numerical Heat Transfer, B21, 217–229.

——— (1992b) Modeling transport processes in nonlinear systems: The example of solidification and convection. In Chaotic Processes in the Geological Sciences: IMA Volume in Mathematics and Its Applications, 41, 221–232.

Rappaz, M., and Voller, V. (1990) Modeling of micro-macrosegregation in solidification processes. Metallurgical Transactions, 21A, 749–754.

Schairer, J.F., and Bowen, N.L. (1938) The system leucite-diopside-silica. American Journal of Science, 35A, 289–309.

Shaw, H.R. (1972) Viscosities of magmatic silicate liquids: An empirical method of prediction. American Journal of Science, 272, 870–893.

——— (1974) Diffusion of $H_2O$ in granitic liquids: I. Experimental data; II. Mass transfer in magma chambers. In A.W. Hofmann, B.J. Gilletti, H.S. Yoder, and R.A. Yund, Eds., Geochemical transport and kinetics, p. 139–170. Carnegie Institution, Washington, DC.

Smith, R.L. (1979) Ash-flow magmatism. Geological Society of America Special Paper, 180, 5–28.

Spera, F.J., Yuen, D.A., and Kirschvink, S.J. (1982) Thermal boundary layer convection in silicic magma chambers: Effects of temperature dependent rheology and implications for thermogravitational chemical fractionation. Journal of Geophysical Research, 87, 8755–8767.

Spera, F.J., Yuen, D.A., and Kemp, D.V. (1984) Mass transfer rates along vertical walls in magma chambers and marginal upwelling. Nature, 310, 764–767.

Spera, F.J., Oldenburg, C.M., and Yuen, D.A. (1989) Magma zonation: Effects of chemical buoyancy and diffusion. Geophysical Research Letters, 16(12), 1104–1108.

Spohn, T., Hort, M., and Fischer, H. (1988) Nucleation simulation of the crystallization of multicomponent melts in thin dikes or sills: I. The liquidus phase. Journal of Geophysical Research, 93, 4880–4894.

Stein, D.J., and Spera, F. (1993) Rheometry of a dacitic melt: Experimental results and tests of empirical models for viscosity estimation. Geophysical Research Letters, 20, 1923–1926.

Taylor, S.R., and McLennan, S.M. (1985) The continental crust: Its composition and evolution, 312 p. Blackwell Scientific, Oxford, U.K.

Trial, A.F., and Spera, F.J. (1988) Natural convection boundary layer flows in isothermal ternary systems: Role of diffusive coupling. International Journal of Heat and Mass Transfer, 31, 941–958.

——— (1990) Mechanisms for the generation of compositional heterogenities in magma chambers. Geological Society of America Bulletin, 10(2), 353–367.

Turner, J.S. (1980) A fluid-dynamical model of differentiation and layering in magma chambers. Nature, 285, 213–215.

——— (1985) Multicomponent convection. Annual Review of Fluid Mechanics, 17, 11–44.

Turner, J.S., and Gustafson, L.B. (1981) Fluid motions and compositional gradients produced by crystallization or melting at vertical boundaries. Journal of Volcanological and Geothermal Research, 11, 93–125.

Urbain, G., Bottinga, Y., and Richet, P. (1982) Viscosity of liquid silica, silicates and aluminosilicates. Geochimica et Cosmochimica Acta, 46, 1061–1072.

van der Molen, I., and Patterson, M.S. (1979) Experimental deformation of partially-melted granite. Contributions to Mineralogy and Petrology, 70, 299–318.

Voller, V.R., Brent, A.D., and Prakash, C. (1989) The modelling of heat, mass and solute transport in solidification systems. International Journal of Heat and Mass Transfer, 32(9), 1719–1731.

——— (1990) Modeling the mushy region in a binary alloy. Applied Mathematical Modeling, 14, 320–326.

Wiebe, R.A. (1993) Basaltic injections into floored silicic magma chambers. Eos, 74, 1–3.

Wolff, J.A., and Storey, M. (1984) Zoning in highly alkaline magma bodies. Geology Magazine, 121(6), 563–575.

Yoo, H., and Viskanta, R. (1992) Effect of anisotropic permeability on

the transport process during solidification of a binary mixture. International Journal of Heat and Mass Transfer, 35, 2335–2346.

## APPENDIX

To facilitate solution of the equations of change, a nondimensionalization was performed by introduction of the following dimensionless variables:

$$\overline{x} = \frac{x}{L} \qquad \overline{y} = \frac{y}{L} \qquad \overline{u} = \frac{uL}{\kappa} \qquad \overline{v} = \frac{vL}{\kappa} \qquad \overline{P} = \frac{L^2 P}{\eta_0 \kappa}$$

$$\overline{t} = t\frac{\kappa}{L^2}\text{St} \qquad \overline{h} = \frac{h - h_{\text{sol}}}{\Delta h} \qquad \overline{h}_s = \frac{h_s - h_{\text{sol}}}{\Delta h}$$

$$\overline{h}_1 = \frac{h_1 - h_{\text{sol}}}{\Delta h} \qquad \overline{T} = \frac{T - T_{\text{sol}}}{T_0 - T_{\text{sol}}}$$

$$\overline{C} = \frac{C - C_0}{C_{\text{sol}} - C_0} \qquad \overline{C}_s = \frac{C_s - C_0}{C_{\text{sol}} - C_0} \qquad \overline{C}_1 = \frac{C_1 - C_0}{C_{\text{sol}} - C_0}.$$

When these variables are substituted into Equations 3–7 the conservation equations take the form

$$\nabla \cdot \mathbf{V} = 0 \tag{A1}$$

$$\frac{1}{Pr}\left(St\frac{\partial u}{\partial t} + \mathbf{V}\cdot\nabla u\right) = -\frac{\partial P}{\partial x} + \nabla\cdot\nabla u - \frac{1}{Da}(u - u_s) \tag{A2}$$

$$\frac{1}{Pr}\left(St\frac{\partial v}{\partial t} + \mathbf{V}\cdot\nabla v\right) = -\frac{\partial P}{\partial y} + \nabla\cdot\nabla v + RaT$$

$$+ RsC_1 - \frac{1}{Da}(v - v_s) \tag{A3}$$

$$St\frac{\partial h}{\partial t} + \mathbf{V}\cdot\nabla h = \nabla^2 h + \nabla^2(h_s - h)$$

$$- \nabla\cdot[(h_1 - h)(\mathbf{V} - \mathbf{V}_s)] \tag{A4}$$

$$St\frac{\partial C}{\partial t} + \mathbf{V}\cdot\nabla C = \nabla\cdot\frac{1}{Le}\frac{D}{D_1}\nabla C + \nabla\cdot\frac{1}{Le}\frac{D}{D_1}\nabla(C_1 - C)$$

$$- \nabla\cdot[(C_1 - C)(\mathbf{V} - \mathbf{V}_s)] \tag{A5}$$

where all bars have been suppressed. The parameters appearing in Equations A1–A5 are defined according to

$$Ra = \frac{\rho_r \alpha g(T_0 - T_{\text{sol}})L^3}{\kappa\eta_0} \qquad Pr = \frac{\eta_0}{\kappa\rho_r} \qquad Da = \frac{K_0}{L^2}$$

$$Rs = \frac{\rho_r g\beta(C_{\text{sol}} - C_0)L^3}{\kappa\eta_0} \qquad St = \frac{c(T_0 - T_{\text{sol}})}{\Delta h} \qquad Le = \frac{\kappa}{D_1} \tag{A6}$$

where $Ra$ is the Rayleigh number, $Pr$ is the Prandtl number, $Da$ is the Darcy number, $Rs$ is the solutal Rayleigh number, $St$ is the Stefan number, and $Le$ is the Lewis number. The convention is adopted that the compositional variable $\overline{C}$ is always expressed in terms of the component that is rejected by the liquidus phase. For example, in all the calculations discussed in this paper, diopside is the liquidus phase, and so $C$ refers to the mass fraction of $KAlSi_2O_6$ (the so-called light component) in the melt, solid, or mixture. The equation of state used is

$$\rho = \rho_r[1 - \alpha(T - T_{\text{sol}}) - \beta(C_1 - C_{1,0})] \tag{A7}$$

where $\rho_r$ is a reference density for melt of composition $C_0$ (the bulk composition) at the eutectic temperature ($T = T_{\text{sol}}$). The

**APPENDIX TABLE** List of symbols

| | |
|---|---|
| $A$ | Identical to enthalpy scale $\Delta h$ defined in Fig. 3 and Eq. 19 in text |
| $C$ | mixture mass fraction $KAlSi_2O_6$ |
| $c$ | isobaric specific heat [J/(kg·K)] |
| $d$ | depth of domain (m) |
| $D$ | chemical diffusivity (m²/s) |
| $Da$ | Darcy number |
| $f_s$ | fraction solid |
| $g$ | acceleration of gravity |
| $h$ | specific enthalpy (J/kg) |
| $h_f^*$ | specific fusion enthalpy of eutectic mixture (J/kg) |
| $\Delta h$ | enthalpy scale defined in Fig. 3 (J/kg) |
| $J$ | species flux (kg/m²s) |
| $k$ | thermal conductivity [J/(m·s·K)] |
| $K$ | permeability (m²) |
| $L$ | width of domain (m) |
| $Le$ | Lewis number |
| $P$ | pressure (N/m²) |
| $Pr$ | Prandtl number |
| $q$ | heat flux (J/m²s) |
| $Ra$ | thermal Rayleigh number |
| $Rs$ | compositional Rayleigh number |
| $R\rho$ | buoyancy number ($\equiv Rs/Ra$) |
| $St$ | Stefan number |
| $T$ | temperature (K) |
| $T_{\text{sol}}$ | eutectic temperature (K) |
| $T_{\text{liq}}$ | liquidus temperature (K) |
| $T_m$ | melting temperature of diopside (K) |
| $T_0$ | initial temperature (K) |
| $t$ | time (s) |
| $u$ | horizontal velocity (m/s) |
| $v$ | vertical velocity (m/s) |
| $\mathbf{V}$ | velocity vector (m/s) |
| $x, y$ | Cartesian coordinates |
| **Greek symbols** | |
| $\alpha$ | isobaric thermal expansivity, (K⁻¹) |
| $\beta$ | isothermal, isobaric compositional expansivity |
| $\kappa$ | thermal diffusivity $\equiv k/\rho c$ (m²/s) |
| $\rho$ | density (kg/m³) |
| $\eta$ | viscosity (kg/ms) |
| $\phi$ | general continuum variable |
| $\tau$ | characteristic time |
| **Subscripts** | |
| $0$ | initial conditions |
| di | diopside |
| f | fusion |
| l | liquid (melt) |
| lc | leucite |
| liq | liquidus |
| m | melting point, pure phase |
| s | solid |
| sol | solidus (eutectic) |
| w | wall |

isobaric expansivity ($\alpha$) and its analog for composition ($\beta$) are defined, respectively, as

$$\alpha \equiv \frac{-1}{\rho}\left(\frac{\partial\rho}{\partial T}\right) \qquad \text{and} \qquad \beta \equiv \frac{-1}{\rho}\left(\frac{\partial\rho}{\partial C_1}\right). \tag{A8}$$

Note that $\beta$ for the light component in a binary system is a positive number. The sign of $Rs$ is determined solely by the sign of $\beta$ because by convention $C_{\text{sol}} - C_0$ is always positive. Finally, there are thermodynamic relations. The enthalpy-temperature relation for a binary eutectic system is depicted in Figure 3. The fictive quantity $\Delta h$, used to define the $h$-$f_s$-$T$-$C_1$ relationship, is defined as

$$\Delta h = \left[1 - \left(\frac{T_{\text{sol}} - T_{\text{liq}}}{T_{\text{sol}} - T_m}\right)\right]h_f^* + \left(\frac{T_{\text{sol}} - T_{\text{liq}}}{T_{\text{sol}} - T_m}\right)h_{f,\text{di}}. \tag{A9}$$

The quantity $h_f^*$ is the fusion enthalpy of eutectic solid (see Table 1). The quantity $\Delta h$ is the amount of energy needed to transform solid of original bulk composition (a mixture of diopside and leucite crystals) into a fictive melt of bulk composition at the solidus temperature. Note that $\Delta h$ depends on $C_0$ implicitly because liquidus temperatures in the system $KAlSi_2O_6$-$CaMgSi_2O_6$ depend on the initial bulk composition. The $h_{f,di}$ represents the fusion enthalpy of diopside crystals, and $T_m$ is the melting temperature of diopside. $T_{liq}$ is the liquidus temperature for the initial bulk composition.